DRUDE-LORENTZ ANALYSIS OF THE OPTICAL PROPERTIES OF THE QUASI-TWO-DIMENSIONAL DICHALCOGENIDES 2H-$NbSe_2$ AND 2H-$TaSe_2$

A Thesis

Presented to

The Graduate Faculty of The University of Akron

In Partial Fulfillment

of the Requirements for the Degree

Master of Science

Dinesh Marasinghe

August, 2018

DRUDE-LORENTZ ANALYSIS OF THE OPTICAL PROPERTIES OF THE QUASI-TWO-DIMENSIONAL DICHALCOGENIDES 2H-$NbSe_2$ AND 2H-$TaSe_2$

Dinesh Marasinghe

Thesis

Approved:

Advisor
Dr. Sasa V. Dordevic

Faculty Reader
Dr. Ben Yu-Kuang Hu

Faculty Reader
Dr. Sergei F. Lyuksyutov

Department Chair
Dr. Chris Ziegler

Accepted:

Dean of the College
Dr. Linda Subich

Dean of the Graduate School
Dr. Chand Midha

Date

ABSTRACT

The reflectivity of a material basically depends on the collisions of free electrons. Existing spectroscopic reflectance data of two dichalcogenide materials, 2H-$NbSe_2$ and 2H-$TaSe_2$, is studied in this work. We analyzed this information with the Drude-Lorentz model for 2D electron gases. Using the program RefFIT, we explored the materials' reflectance and the conductivity and their dependance on temperature across frequencies ranging from infrared to ultraviolet. We examined both the in-plane (ab-plane) and out-of-plane (c-axis) components. In both materials, the ab-plane had greater reflectance and conductivity, with 2H-$NbSe_2$ having the largest of both quantities. The anisotropy-direction dependence-effects are most pronounced in 2H-$TaSe_2$. When frequency increased, collisions of free elections increased, decreasing the reflectance and conductivity. We also determined that the reflectance and the conductivity of the materials decreased with increased temperature for the same reason. Once the plasma edge was reached, interband transition occurred, causing an increase in conduction electrons and a decrease in both reflectance and conductivity.

ACKNOWLEDGEMENTS

First, I would like to give my sincere gratitude to my advisor Dr. Sasa V. Dordevic for his valuable guidance, advice, and motivation during my research work and also the MS study. I really appreciate his constant support in all the time of my research and thesis writing. I want to say "Thank you so much Dr. Sasa, for the great support!".

Thank you Dr. Hu and Dr. Sergei for being a part of my thesis committee, thank you Dr. Jutta for all your help throughout my masters, thank you Matt for reading my thesis, and thank you Prabuddha for your great support during my research.

I give my heartiest thank to my parents, my lovely wife Nirmala and my son Theviru for supporting me in many ways to achieve my academic goals.

I thank to all my professors, my colleagues for their valuable suggestions for my research and support throughout my MS study.

TABLE OF CONTENTS

LIST OF TABLES

LIST OF FIGURES

CHAPTER I

INTRODUCTION

Electronic and magnetic properties of the two dimensional (2D) electron gas have been at the focus of condensed matter physics for many decades[2, 3]. Some dichalcogenide classes can be used for the investigation of the 2D electron gas in the frequency domain. A chalcogenide is a chemical compound which consists of at least one chalcogen anion and at least one more electropositive element. These chalcogens are located in group 16 of the periodic table. The term chalcogenide is commonly reserved for sulfides, selenides, tellurides, and polonides. These dichalcogenide compounds belong to a large class of conductors called "bad metals" (with a mean free path smaller than the lattice constant along c-axis), which also includes the superconducting cuprates. Many metal ores exist as chalcogenides[4, 5, 6].

Large single crystals of various dichalcogenides permit investigation of carrier dynamics using infrared spectroscopy and optical spectroscopy[3]. The layered crystal structure results in strong anisotropy between in-plane (ab-plane) and inter-plane (c-axis) response. In these systems the 2D electron gas reveals charge-density-wave (CDW) instabilities occurring at temperatures above the critical temperature (T_c) of the superconducting transition. This particular feature of dichalcogenides is especially intriguing in view of the anomalous properties of other class of strongly anisotropic

layered materials, such as the high-T_c cuprate superconductors (HTC).

Magnetic and orbital degrees of freedom play an important role in dichalcogenides. Therefore, this class of materials allows one to isolate the effects associated with density wave instabilities and to explore the role of these effects for the dynamics of the correlated quasi-2D electron gas.

In this study, two particular dichalcogenides, 2H-$NbSe_2$ and 2H-$TaSe_2$ were analyzed; mainly the reflectivity and the optical conductivity of these materials were studied in this report using the Drude model and Lorentz model. For low frequencies, the reflectivity is high because fewer electrons are in the conduction band; therefore the number of collisions is less. But for higher frequencies, interband transition occurs and the number of collisions in the conduction band increases, resulting in lower reflectivity at higher frequencies. The program RefFIT was used to fit the Drude-Lorentz model to the graphs with optical data. We have fitted the reflectivity and the optical conductivity as functions of frequency for both in-plane (ab-plane) and inter-plane (along c-axis) cases. Reflectance data was also taken for several temperatures. Reflectivity decreases as temperature increases and the resulted fits have metallic behavior. Further information can be found in chapter 6.

CHAPTER II

MATERIALS

2.1 2H-$TaSe_2$

2H-$TaSe_2$ is a metal that belongs to the transition metal dichalcogenides, a group know as quasi two dimensional conductors[7]. They have a layered structure where the triangular lattice layer of metal (Ta) is sandwiched by two triangular lattice layers of selenide (Se). The layers are stacked together via van der Waals interaction and can be exfoliated into 2D. 2H-$TaSe_2$ is an incommensurate charge density waves (CDW) system at $\sim$ 120 K, a commensurate CDW system at $\sim$ 90 K and a superconductor with critical temperature $T_c \sim 0.1$ K.

2.2 2H-$NbSe_2$

2H-$NbSe_2$ is a layered transition metal dichalcogenide that has generated much recent interest as a model system for understanding the interplay of the CDW and superconductor (SC) phases[8, 9, 10]. It undergoes a phase transition to an incommensurate, triangular change density wave phase at a temperature $T_{CDW} \sim 33$ K. It also becomes a prototypical anisotropic S-wave superconductor below a temperature $T_{SC} \sim 7.2$ K. Though $NbSe_2$ has been extensively studied by thermodynamic and

spectroscopic probes, several key questions pertaining to the CDW remain. In particular, questions regarding the CDW wave vector, the magnitude of the CDW gap and the role of Fermi Surface nesting remain unresolved.

2H-$NbSe_2$ has a layered hexagonal structure. The unit cell consists of two sandwiches of Se-Nb-Se. The crystal typically cleaves between the weakly coupled neighboring Se layers, and the top Se layer is imaged by Scanning Tunneling Microscope (STM).

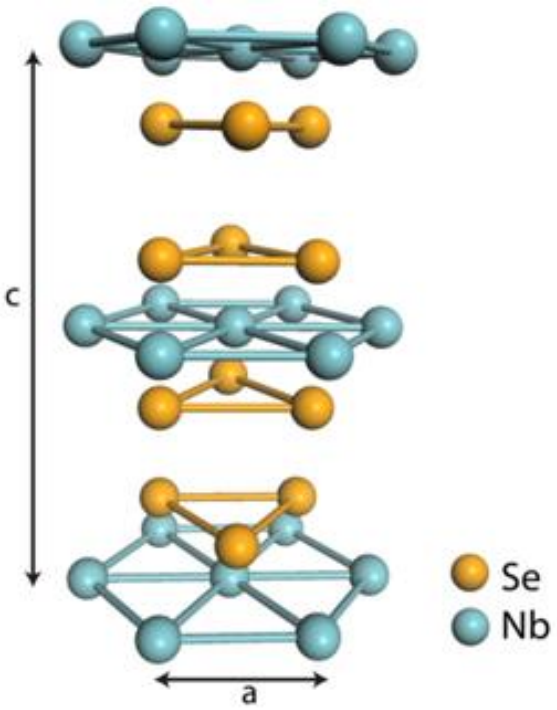

Figure 2.1: Crystal structure of 2H-$NbSe_2$ (http://hoffman.physics.harvard.edu/)

2.3 Resistivity of the materials

This section will discuss the temperature dependence of the resistivity of both materials.

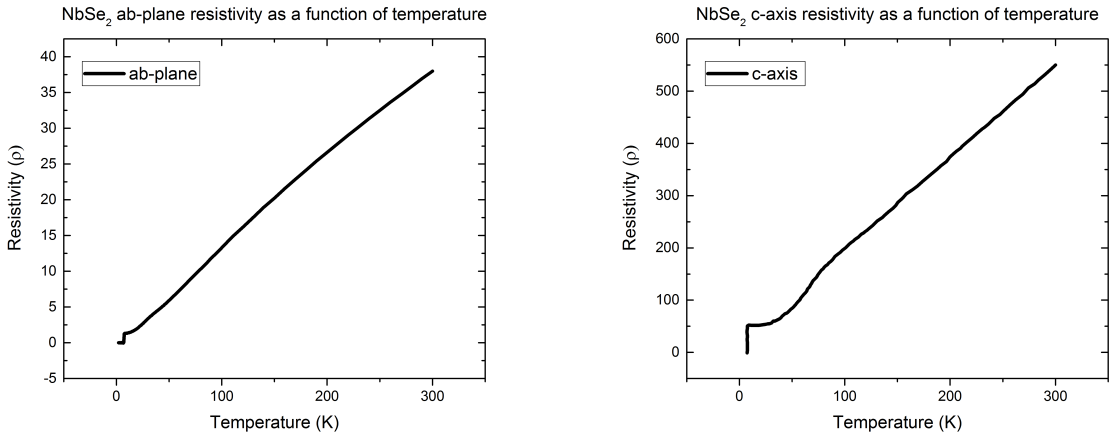

Figure 2.2: Resistivity data of $NbSe_2$ for *ab*-plane and *c*-axis.

Figure 2.2 shows the resistivity of $NbSe_2$ as a function of temperature for *ab*-plane and *c*-axis, respectively. Both graphs have similar shape, with resistivity decreasing as temperature decreases until finally the materials become superconductive (zero resistivity). The focus of this study the CDW behavior of these materials. The Charge Density Wave (CDW) gap is expected in these materials to be only along certain wave-vectors, while remaining gapless (and metallic) along other regions of the Fermi surface. However, the electronic structure of these two systems in the CDW state is still questionable[11].

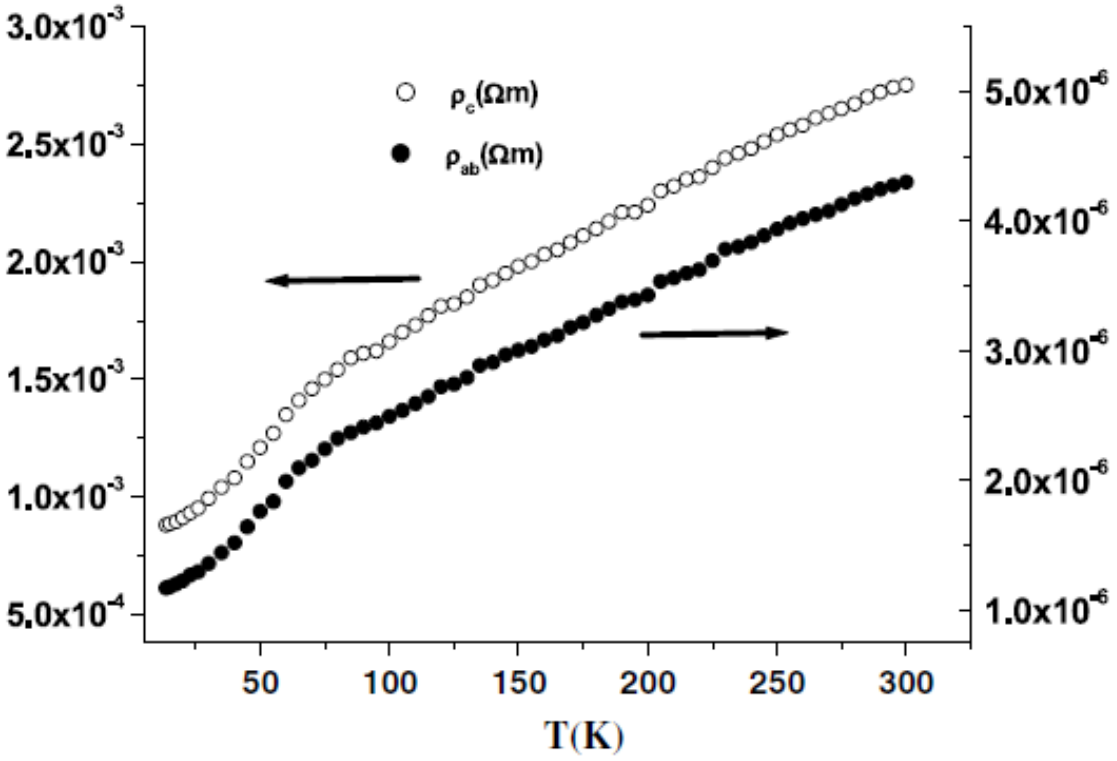

Figure 2.3: Resistivity data of $TaSe_2$ for ab-plane and c-axis.

Figure 2.3 indicates the resistivity of $TaSe_2$ for ab-pane and c-axis. Here also the shape of both graphs are the same. A notable feature of both graphs is the drop in resistivity at T$\sim$ 75 K.

The c-axis resistivity is higher than the ab-plane resistivity, the gap between ab-plane resistivity and the c-axis resistivity of $NbSe_2$ is higher than that of $TaSe_2$.

2.4 Experimental Techniques

Infrared and optical spectroscopy are commonly used experimental techniques to determine a solid's response to electromagnetic radiation, phonons, anharmonicity, and electron-lattice coupling[12, 13]. Optical frequencies refer to the ultraviolet and visible light pertaining 12,500-5,0000 cm^{-1}. When materials interact with radiation at these frequencies, energy excitationof the outer shell electrons allows exploration of electron inter-band transition and plasma oscillations. In contrast, the infrared range is lower in frequency compared to the optical range. When in the lower frequency infrared range (30 - 12,500 cm^{-1}) the material could absorb the energy which can lead to plasma oscillations, lattice vibrations, and electron intra-band transitions.Thus, the broad frequency range, 30-50000 cm^{-1} allows for understanding of the charge dynamics, low-energy excitation, and electronic band structure[14, 15, 16, 17].

In this analysis, we considered the reflectivity data of previous noted materials, $NbSe_2$ and $TaSe_2$ for two different directions, in-plane (ab-plane) and inter-plane (c-axis). All the data was previously taken using Fourier transform infrared spectroscopy (FTIR) and UV visible spectroscopy. The mechanism of this FTIR is through a Michelson interferometer. Figure 2.4 and figure 2.5 show the actual instrument and the mechanism, respectively. Figure 2.6 and 2.7 show the actual instrument and mechanism of UV visible spectrometer.

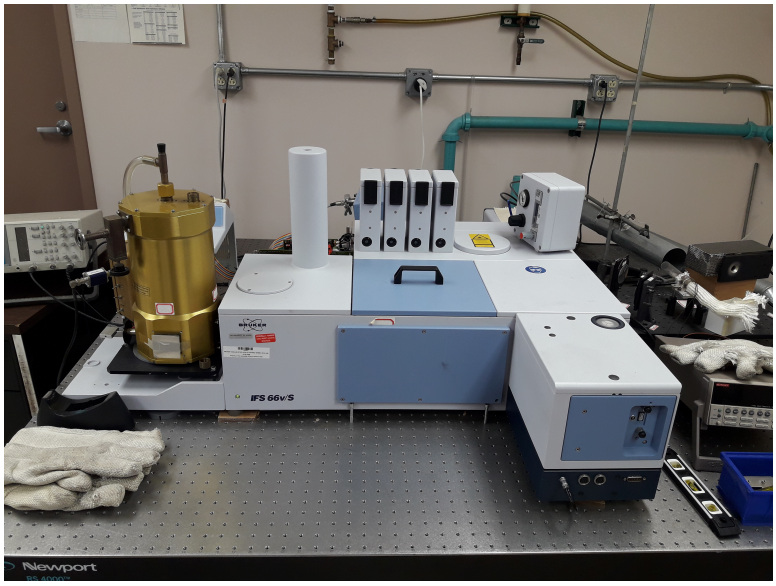

Figure 2.4: Bruker IFS 66v/S - Actual instrumentation.

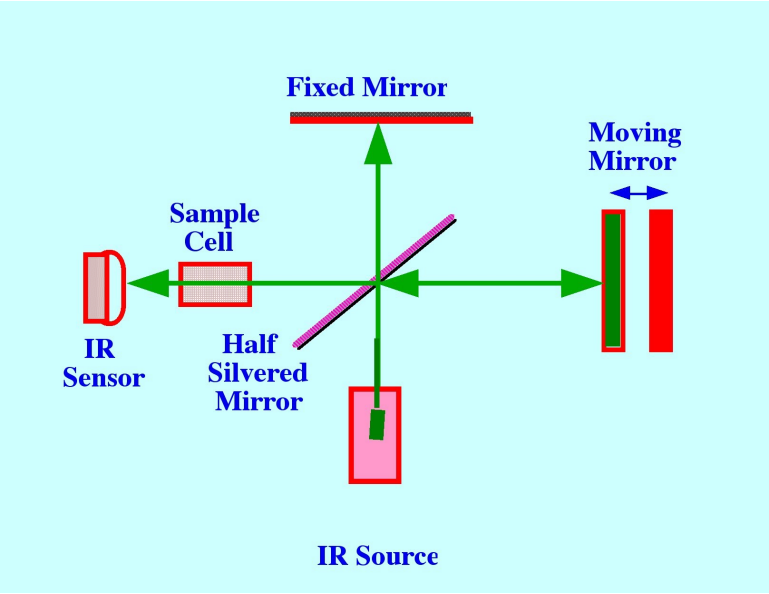

Figure 2.5: Mechanism of FTIR.

Figure 2.6: Cary 300 - Actual instrumentation of UV visible spectrometer.

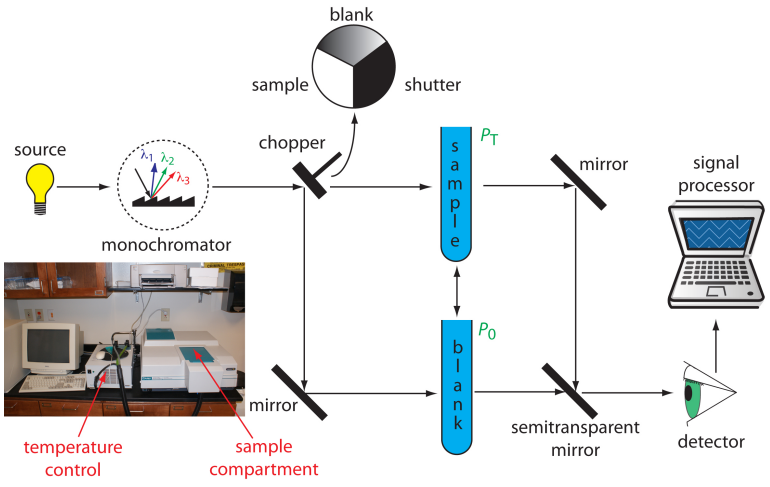

Figure 2.7: Mechanism of UV visible spectrometer.

Then, the Drude-Lorentz model was used to fit the data using software called "RefFIT", a program designed to analyze the optical spectra of solids, specifically frequency dependent optical quantities such as reflection, transmission, and ellipsometry outputs. Some important features of RefFIT program and how to use it are described in chapter 3. The analyzed results of the Drude-Lorentz fits and comparison of results are presented in the Results and Discussion chapter.

CHAPTER III

THEORY

In this chapter, I will discuss the basic theorems related to the classical aspect of matter's optical properties. The Lorentz and Drude models play a significant role in determining optical properties of matter. The Lorentz model describes insulators and the Drude model describes metals and semiconductors[18].

3.1 Lorentz Model

In 1905 The dielectric responses of insulators were described by the Lorentz model. The equation of motion of an electron in an oscillating electric field $\vec{E}$ with frequency ω is

$$m\frac{d^2X}{dt^2} = F_{\text{DRIVING}} + F_{\text{DAMPING}} + F_{\text{SPRING}} \tag{3.1}$$

$$m\frac{d^2X}{dt^2} = F_{\text{DRIVING}} - m\Gamma_0\frac{dX}{dt} - m\omega_0^2 X \tag{3.2}$$

$$m\left[\frac{d^2X}{dt^2} + \Gamma_0\frac{dX}{dt} + \omega_0^2 X\right] = qE = qE_0e^{-i\omega t} \tag{3.3}$$

Here, m is the electron mass, X is the possition of the electron relative to the atom, Γ_0 is the damping coefficient and also the bandwidth, ω_0 is the resonance

frequency of an electron, q is the absolute value of the electron charge, ω is the angular frequency of the time-varying electric field, and E_0 is the amplitude of the electric field[18, 19].

Assuming the solution to Eq.(3.3) is

$$X = X_0 e^{-i\omega t} \tag{3.4}$$

then Eq.(3.4) is substituted into Eq.(3.3). The amplitude of the displacement X_0 is then found as

$$m\big[-\omega^2 X_0 - i\omega\Gamma_0 X_0 + \omega_0^2 X_0]e^{-i\omega t} = qE_0 e^{-i\omega t} \tag{3.5}$$

$$X_0 = \frac{qE_0}{m\big(\omega_0^2 - \omega^2 - i\omega\Gamma_0\big)} \tag{3.6}$$

The polarization $\vec{P}$ can be written as

$$\vec{P} = NqX = \big(\epsilon - \epsilon_0\big)\vec{E} \tag{3.7}$$

$$NqX_0 e^{-i\omega t} = \big(\epsilon - \epsilon_0\big)E_0 e^{-i\omega t} \tag{3.8}$$

substituting Eq.(3.6) into Eq.(3.8) gives

$$Nq\frac{qE_0}{m\big(\omega_0^2 - \omega^2 - i\omega\Gamma_0\big)}e^{-i\omega t} = \big(\epsilon - \epsilon_0\big)E_0 e^{-i\omega t} \tag{3.9}$$

Suppose we have N oscillators in a unit volume, and Nf_i of them have an Eigen frequency ω_j, where f_i is the oscillator strength. Therefore, the dielectric function of this group of oscillators from Eq.(3.9) is

$$\epsilon\big(\omega) = \epsilon_0 + \frac{Nq^2}{m}\sum_j \frac{f_j}{\big(\omega_j^2 - \omega^2 - i\omega\Gamma_j\big)} \tag{3.10}$$

If we consider one particular oscillator at $\omega = 0$, we define ϵ_l and ϵ_u as the dielectric functions at sufficient lower and higher frequencies by

$$\epsilon_0 = \epsilon_u \tag{3.11}$$

$$\epsilon\big(0\big) = \epsilon_l \tag{3.12}$$

Then, substituting Eqs.(3.11) and (3.12) in Eq.(3.10) we get

$$\epsilon_l = \epsilon_u + \frac{Nq^2}{m\omega_0^2} \tag{3.13}$$

$$(\epsilon_l - \epsilon_u)\omega_0^2 = \frac{Nq^2}{m} \tag{3.14}$$

Substituting Eq.(3.14) in Eq.(3.10), we get

$$\epsilon_l = \epsilon_u + \frac{\big(\epsilon_l - \epsilon_u)\omega_0^2}{\big(\omega_0^2 - \omega^2 - i\omega\Gamma_0\big)} \tag{3.15}$$

$$\frac{\epsilon_l}{\epsilon_u} = 1 + \frac{\left(\frac{\epsilon_l}{\epsilon_u} - 1\right)\omega_0^2}{\big(\omega_0^2 - \omega^2 - i\omega}\Gamma_0) \tag{3.16}$$

When $\Gamma_0^2 << \omega_L^2 \approx \omega_0^2$, the Lyddane-Sachs-Teller relation is

$$\frac{\epsilon_l}{\epsilon_u} = \frac{\omega_L^2}{\omega_0^2} \tag{3.17}$$

Then, the dispersion relation can is obtained by substituting Eq.(3.17) into Eq.(3.16)

$$\epsilon_l = \epsilon_u\left[1 + \frac{\omega_L^2 - \omega_0^2}{\big(\omega_0^2 - \omega^2 - i\omega\Gamma_0\big)}\right] \tag{3.18}$$

where ω_L is the frequency of the longitudinal wave.

3.2 Drude Model

The Drude free electron model of metals considers the valence electrons of atoms to be free[20]. Drude has mentioned about the behavior of the electrons in the metals. In his words, "Electrons in metals are loosely connected to their cores and can perform quasi-free movements". This is plasma-like behavior. If an electric field $\vec{E} = E_0 e^{-i\omega t}$ is applied to a free electron gas, the electrons experience acceleration force $\left(m^* \frac{d^2X}{dt^2}\right)$ and electron collisions $\left(m^* \tau^{-1} \frac{dX}{dt}\right)$. Then, since no restoring force is applied to the free electrons in the material as the electrons are not bound to the nuclei, the natural frequency of $\omega_0 = 0$. Now we can write equation (3.3) as follows.

$$m^* \left[\frac{d^2X}{dt^2} + \tau^{-1} \frac{dX}{dt} \right] = qE = qE_0 e^{-i\omega t} \tag{3.19}$$

Where τ is the average time interval between one scattering with another free electrons (normally around 10^{-14} s) and m^* is the effective mass of an electron. Then, assuming the Eq.(3.19) has the form of Eq.(3.4) and substituting Eq.(3.4) into Eq.(3.19), X_0 can be obtained as

$$m^* \big[-\omega^2 X_0 - i\omega\tau^{-1} X_0 \big] e^{-i\omega t} = qE_0 e^{-i\omega t} \tag{3.20}$$

$$X_0 = \frac{qE_0}{m^* \big(-\omega^2 - i\omega\tau^{-1} \big)} \tag{3.21}$$

From the polarization equation(3.8), we have

$$NqX_0 e^{-i\omega t} = \big(\epsilon - \epsilon_0 \big) E_0 e^{-i\omega t} \tag{3.22}$$

Then, substituting Eq.(3.8) into Eq.(3.21), the dielectric function of this material can be found as

$$\epsilon = \epsilon_0 - \frac{Ne^2}{m^*\omega\left(\omega + i\tau^{-1}\right)} \tag{3.23}$$

In the low frequencies ($\omega \approx 0$), Eq.(3.23) becomes

$$\epsilon = \epsilon_0 + i\frac{Ne^2\tau}{m^*\omega} \tag{3.24}$$

If the electrical conductivity σ is defined as

$$\sigma = \frac{Ne^2\tau}{m^*} \tag{3.25}$$

by substituting Eq.(3.25) into Eq.(3.24), we get

$$\epsilon = \epsilon_0 + i\frac{\sigma}{\omega} \tag{3.26}$$

for high frequencies, Eq.(3.23) becomes

$$\epsilon = \epsilon_0 - \frac{Ne^2}{m^*\omega^2} \tag{3.27}$$

Let's consider the plasma frequency ω_p as

$$\omega_p = \sqrt{\frac{Ne^2}{m^*\epsilon_0}} \tag{3.28}$$

Then, substituting Eq.(3.28) into Eq.(3.27) gives

$$\epsilon = \epsilon_0 - \epsilon_0\frac{\omega_p^2}{\omega^2} \tag{3.29}$$

$$\epsilon = \epsilon_0\left(1 - \frac{\omega_p^2}{\omega^2}\right) \tag{3.30}$$

As ω_p is plasma frequency, $\hbar\omega_p$ is located in either the visible or ultraviolet photon energy range. Real metals behave like ideal metals below this energy region, and their optical reflectivity tends to be close to unity.

The Drude model can be applied to all materials if the frequencies are sufficiently high. When ω becomes infinite, ϵ equals ϵ_0 and the refractive index becomes unity. That's why we cannot see any good mirrors or lenses in X-ray or γ-ray regions[18, 19, 21].

3.3 Infrared and Optical spectroscopy

Infrared and optical spectroscopy can be used to investigate and analyze the responses of a solid to electromagnetic (EM) waves[22]. Interactions between a solid and EM wave are described as prime response functions. These function are given by the complex dielectric function $\tilde{\epsilon}(\omega)$ and the complex optical conductivity $\tilde{\sigma(\omega)}$[22]. The electric polarization and current induced response to an applied electric field are described by these two response functions. They cannot be determined directly through experimental method, but the reflectance $R(\omega)$ can be measured by a reflectance experiment and then the functions can be calculated by applying a transformation. In this section, the theory behind the optical conductivity and dielectric function are addressed briefly.

3.3.1 Optical Definitions

Wave equations can be obtained by using Maxwell's equations in terms of the electric and magnetic field. The spatial and time-dependent electric and magnetic field vectors can be given by as a propagating plane wave as follows[3, 23].

$$\vec{E} = \vec{E_0} e^{i(\vec{k}.\vec{r}-\omega t)} \text{ and } \vec{B} = \vec{B_0} e^{i(\vec{k}.\vec{r}-\omega t)} \tag{3.31}$$

where $\vec{k}$ and ω are the wave vector and frequency, respectively. As in an absorbing medium, the wave vector $\vec{k}$ is proportional to the complex refractive index $\tilde{n}(\omega)$. Then, following equation can be written

$$k = \tilde{n}(\omega)\frac{\omega}{c} \tag{3.32}$$

where c is the speed of light and

$$\tilde{n}(\omega) = n(\omega) + ik(\omega) \tag{3.33}$$

where $n(\omega)$ is the refractive index (the real part of the complex refractive index) and $k(\omega)$, known as the extiction coefficient, is its imaginary part[20]. The refractive index $n(\omega)$ is the ratio of the speed of light c in vacuum to its speed in a given medium. The extinction coefficient $k(\omega)$ is directly related to the absorption coefficient of the material. The absorption coefficient describes the attenuation of a light beam incident upon a material.

If the magnetic permeability μ of a medium is 1 at optical frequencies, the relationship between the complex refractive index $\tilde{n}(\omega)$ of the medium and its complex dielectric function $\tilde{\epsilon}(\omega)$ can be written using the wave equation as follows[20]

$$\tilde{n}(\omega) = \sqrt{\tilde{\epsilon}} \tag{3.34}$$

The complex dielectric function and the optical conductivity can be expressed as

$$\tilde{\epsilon} = \epsilon_1 + i\epsilon_2 \text{ and } \tilde{\sigma} = \sigma_1 + i\sigma_2 \tag{3.35}$$

From these equations, the real and the imaginary parts of $\tilde{n}$ and $\tilde{\epsilon}$ are related by

$$\epsilon_1 = n^2 - k^2 \text{ and } \epsilon_2 = 2nk \tag{3.36}$$

or, inversely

$$n = \sqrt{\frac{\sqrt{(\epsilon_1^2 + \epsilon_2^2)} + \epsilon_1}{2}} \text{ and } k = \sqrt{\frac{\sqrt{(\epsilon_1^2 + \epsilon_2^2)} - \epsilon_1}{2}} \tag{3.37}$$

The complex dielectric function is directly proportional to the optical conductivity through

$$\tilde{\epsilon}(\omega) = 1 + \frac{4\pi\tilde{\sigma}(\omega)}{\omega} \tag{3.38}$$

and the real and imaginary parts are

$$4\pi\sigma_1 = \omega\epsilon_2 \text{ and } 4\pi\sigma_2 = \omega(\epsilon_1 - 1) \tag{3.39}$$

The complex reflectivity $\tilde{r}(\omega)$ can be defined as the ratio of reflected to incident electric fields

$$\tilde{r}(\omega) = \frac{E_{(\text{ref})}}{E_{(\text{inc})}} = \rho(\omega)e^{i\theta(\omega)} = \frac{\tilde{n}-1}{\tilde{n}+1} \tag{3.40}$$

where $\rho(\omega)$ and $\theta(\omega)$ are amplitude and phase respectively[24]. The reflectance $R(\omega)$ is a dimensionless real quantity and is expressed as the ratio of the reflected field intensity to the incident field intensity. So, it can be written in terms of the dielectric function as

$$R(\omega) = \tilde{r}\tilde{r}^* = \rho^2 = |\frac{\tilde{n}-1}{\tilde{n}+1}|^2 = |\frac{\sqrt{\tilde{\epsilon}}-1}{\sqrt{\tilde{\epsilon}}+1}|^2 \tag{3.41}$$

This is an important equation for modelling the reflection curves with known dielectric function. The reflectance $R(\omega)$ can be expressed in terms of n and k as

$$R(\omega) = \frac{(n-1)^2+k^2}{(n+1)^2+k^2} \tag{3.42}$$

3.4 Fourier Transform Infrared Spectroscopy (FTIR)

FTIR is a technique to obtain the infrared spectrum of absorption or emission of a solid, liquid or gas. High spectral resolution data is collected by FTIR over a wide spectral range. The goal of FTIR is to measure how well a sample absorbs light at each wavelength. "Dispersive spectroscopy" is a direct way to accomplish this. It

allows monochromatic light to hit a sample, then measure how much of the light was absorbed for each different wavelength.

FTIR spectroscopy is a less intuitive way to obtain the same information. Rather than shining a monochromatic beam of light at the sample, this technique shines a beam containing many frequencies of light at once and measures how much of that beam is absorbed by the sample. Then, the beam is modified to contain a different combination of frequencies to give a second data point. This process is repeated many times. Then, all the data is taken by a computer and used for many frequency combos to determine the absorption at each and every wavelength.

The monochromatic light beam mentioned above is generated by starting with a broadband light source that contains the full spectrum of wavelengths to be measured. Light is shined into a certain configuration of mirrors, one of which is moved by a motor (this is known as "Michelson interferometer"). As the mirror moves, each wavelength of light in the beam is periodically blocked and transmitted, by the Michelson interferometer due to wave interference. The beam coming from the interferometer has a different spectrum due to the modulate of different wavelength at different rates. Computer processing is required to process the data which are taken from the FTIR. For the analysis, a well-know algorithm "Fourier transform" is used. Therefore, this is called "Fourier-transform spectroscopy".

Prior to 1966, spectrocopists who measure the spectra interferometrically used the same basic algorithm for their computations. They are now known as classical, conventional, or discrete Fourier transform. Although most scientists now use

the fast Fourier transform technique, the conventional Fourier transform leads to a more complete understanding of the data[21].

CHAPTER IV

REFFIT PROGRAM

4.1 RefFIT

RefFit is software which is used to fit optical spectra. It was introduced as a home made tool by Alexy Kuzmenko, a research scientist at the University of Geneva, Switzerland. Initially, this was a DOS program for Drude-Lorentz fitting of the reflection coefficient, but later it was developed into Windows application. This fast and flexible software models spectral data of dielectric function from various kinds of experiments, such as reflectivity, transmission, ellipsometry etc., using the Drude-Lorentz, Kramer-Kronig, and other physical models. The basic principles of RefFit are: it should be possible combine different types of spectra and fit them simultaneously, a user should be able to see in real time how the fitting occurs and the program should run fast as possible and there should be a macro language for routing operations[25].

RefiFit is specially designed to analyze optical spectra of solids. Normally, optical spectra means frequency-dependent optical quantities. For example, optical spectra are the frequency-dependent reflectivity $R(\omega)$, which can be directly measured, and optical conductivity $\sigma(\omega)$, which is not directly measured but derived

from experimental data. The primary goal of spectra analysis, that RefFit does, is to get information about the material's dielectric function on the basis of optical spectra. It is done by the fitting these spectra using a model of the dielectric function with a set of adjustable parameters. These parameters are varied in order to obtain the best match between the experimental and calculated data points.

The Fresnel formula is used to analyze the data in this software, and the Drude-Lorentz model is the foundation of this formula. This formula can be written as follows

$$R = |\frac{1 - \sqrt{\epsilon}}{1 + \sqrt{\epsilon}}|^2 \tag{4.1}$$

where R is the normal-incident reflectivity.

4.2 How to use RefFit

As mentioned above RefFit, is a tool to fit optical data. In this section, I will give a brief introduction about "How to use RefFit". The very first interface of the software is given in Figure 4.1.

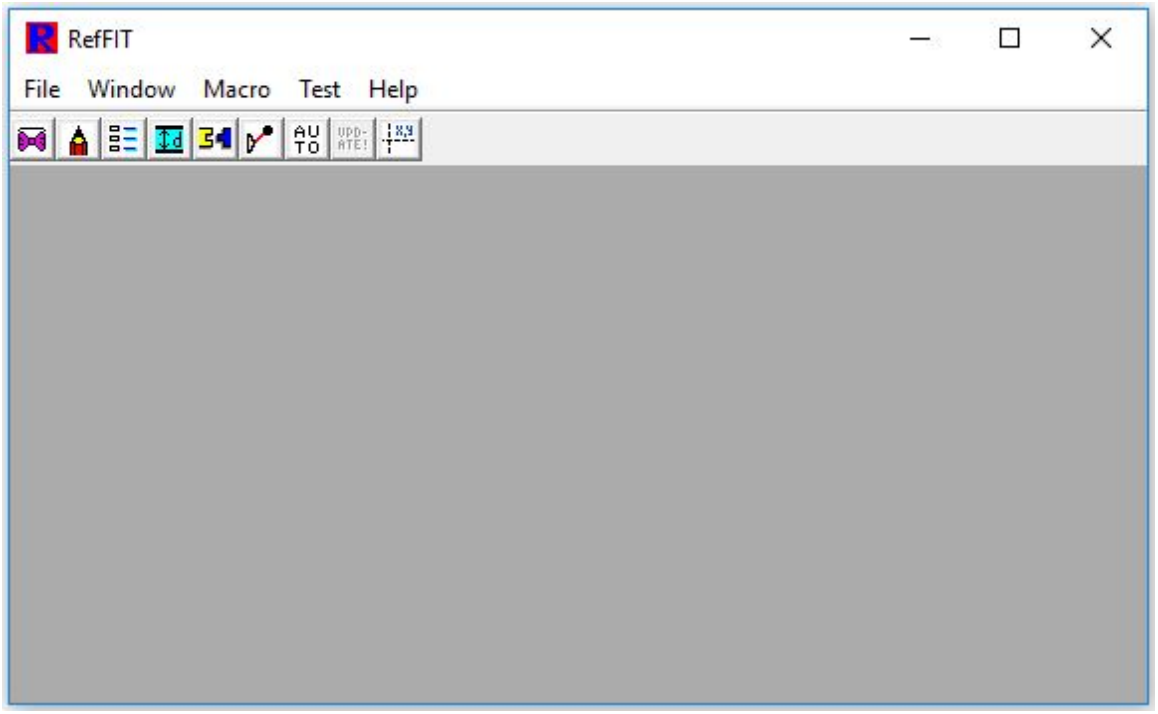

Figure 4.1: First interface of the RefFit software.

The dataset manager is used to load the data into program. Using this interface, we can change the quantity and cutting range of the dataset. Figure 4.2 shows before loading the data and Figure 4.3 shows after loading the data.

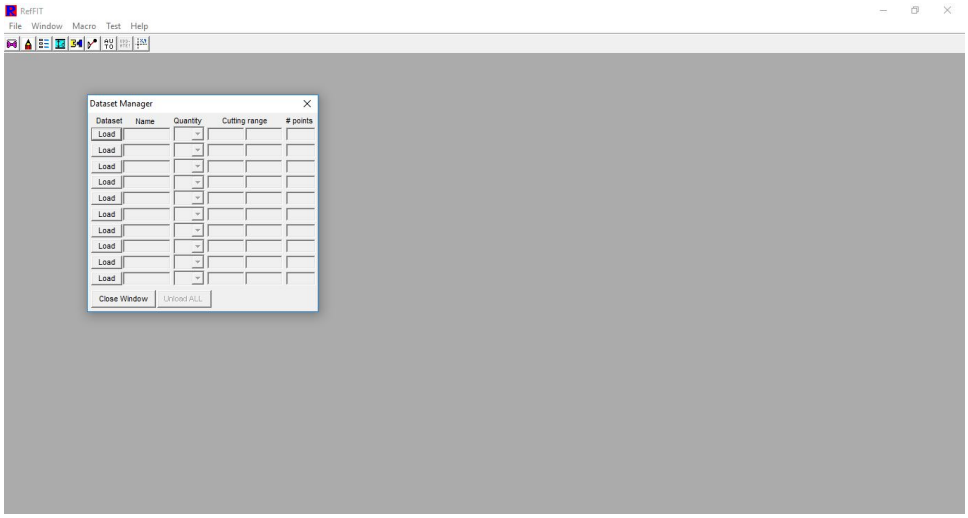

Figure 4.2: Dataset manager interface before loding the data.

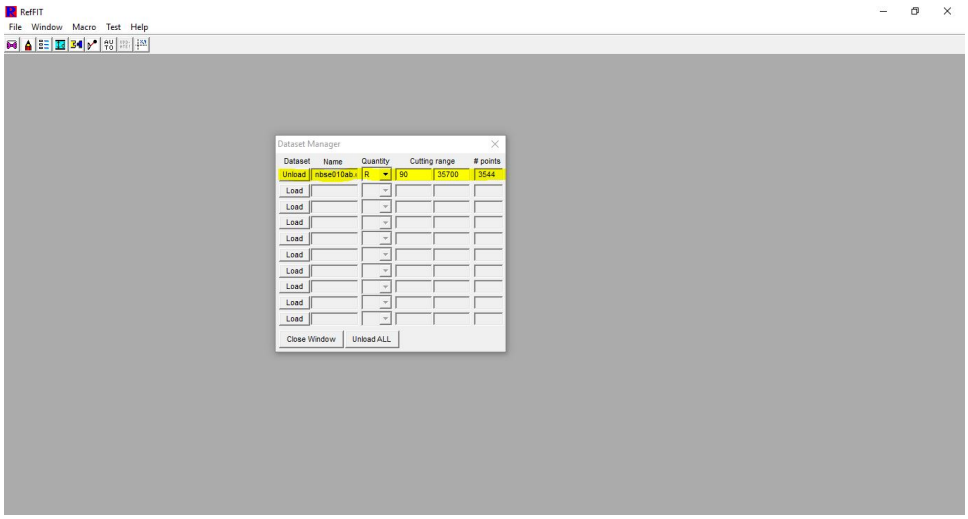

Figure 4.3: Dataset manager interface after loading the data.

Then we have to open a graph to plot the dataset. By double clicking on the graph, we get the contents window and have to transfer the data set from "Available curves" to "Graph curves" using the right arrow in between the "Available curves" and "Graph curves". Figure 4.4 shows the graph window and Figure 4.5 shows the contents window.

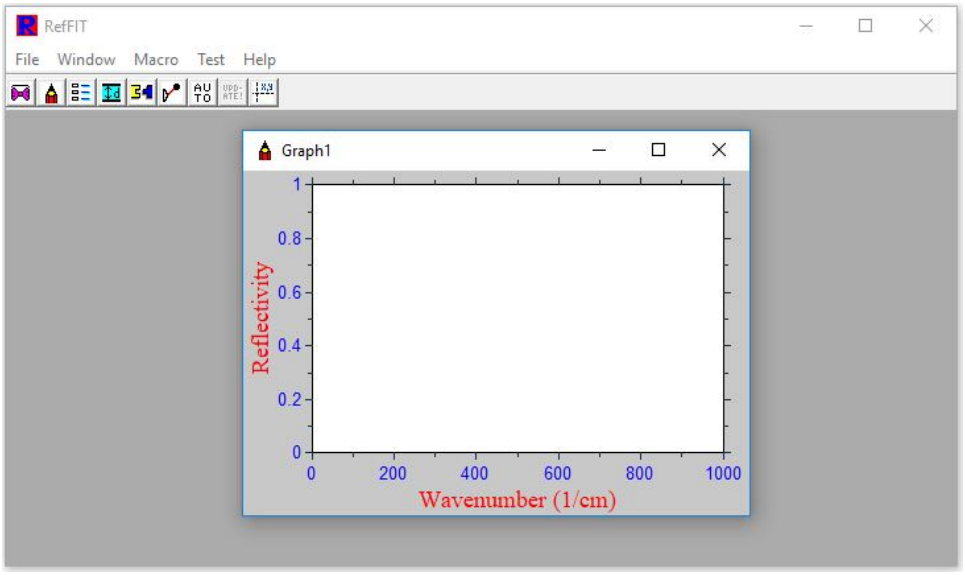

Figure 4.4: Interface with the graph window.

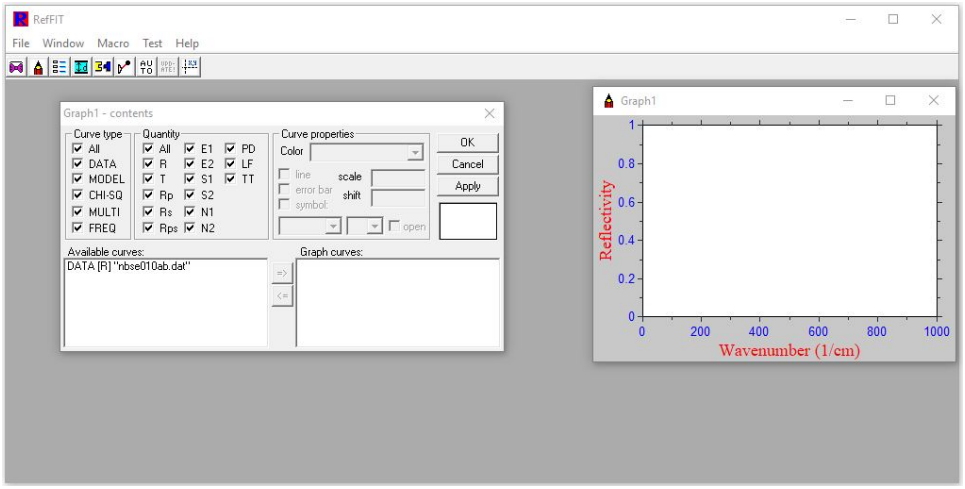

Figure 4.5: Interface with the contents window.

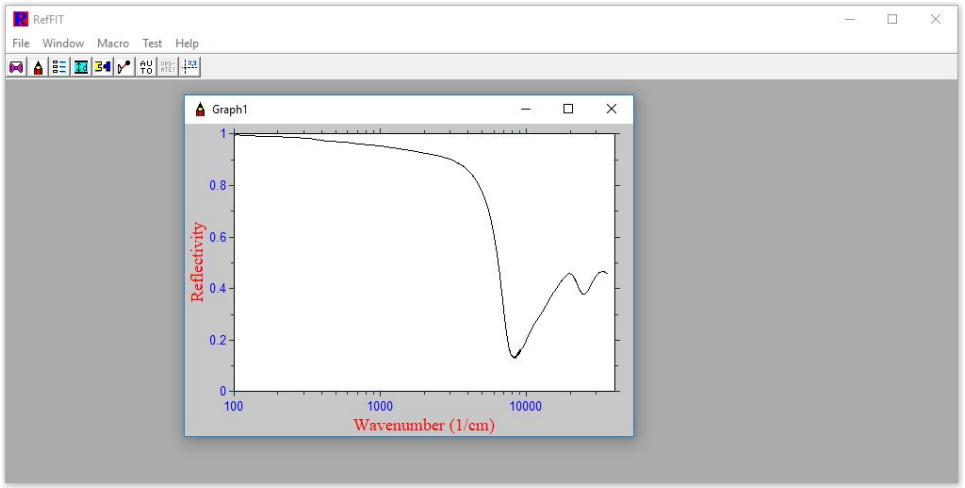

Figure 4.6: Loaded data to the graph.

After loading the data to the graph as shown in figure 4.6, we have to draw the curve using the Drude and Lorentz modes to analyze the data set. Figure 4.7 shows the model window and with that the parameter control window will automatically appear. Again, by double clicking on the graph, we can import the model to the graph using the contents window as done previous.

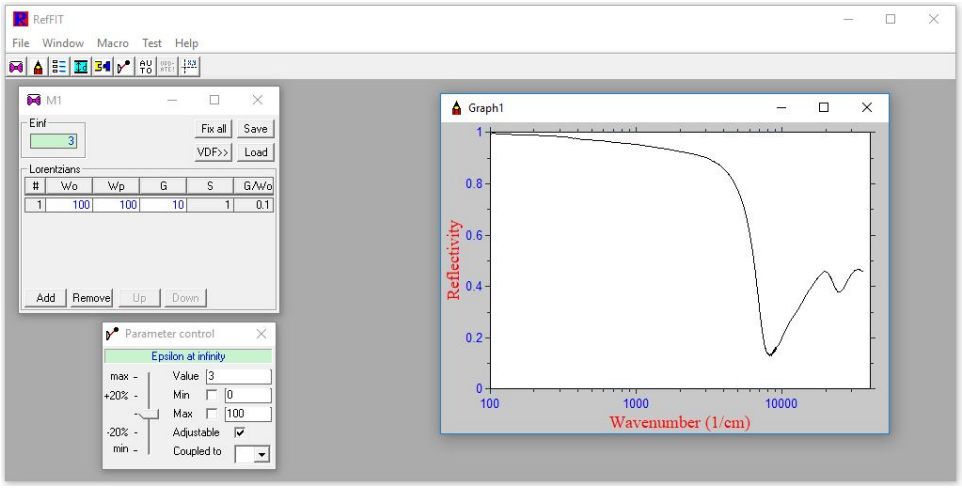

Figure 4.7: Model window and parameter control window.

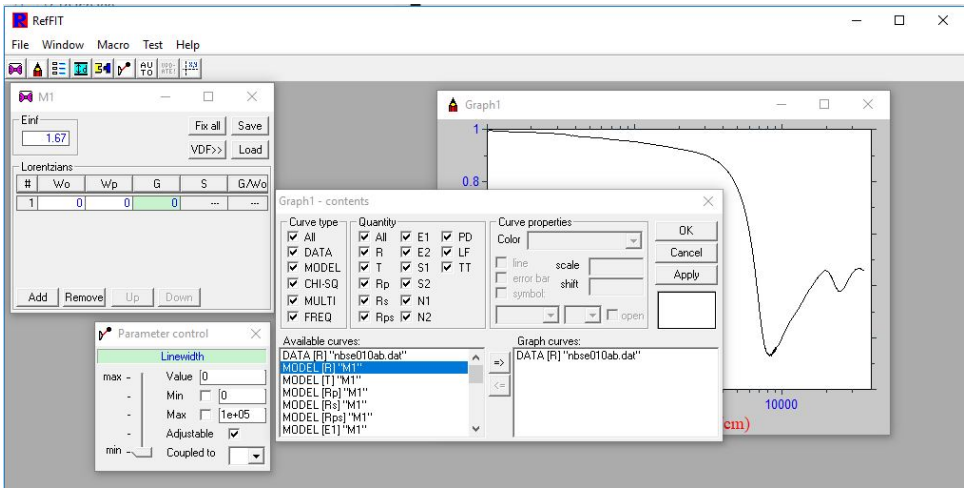

Figure 4.8: Model window and parameter control window with the contents window.

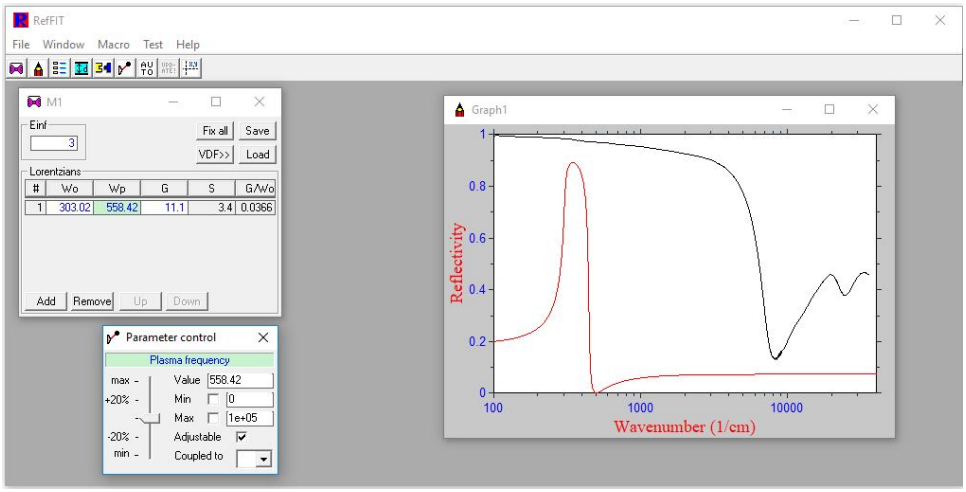

Figure 4.9: Inserting Drude and Lorentz models to the graph.

We can add more modes to the graph to get a better curve. But, using less number of modes make analysis simpler. Therefore, it is better to keep moderate number of modes to get the fitting curve. After adding some Drude and Lorentz modes we get a better curve and then we can use these models to analyze the data. Figure 4.10 shows the well fitted curve using few Drude and Lorentz modes.

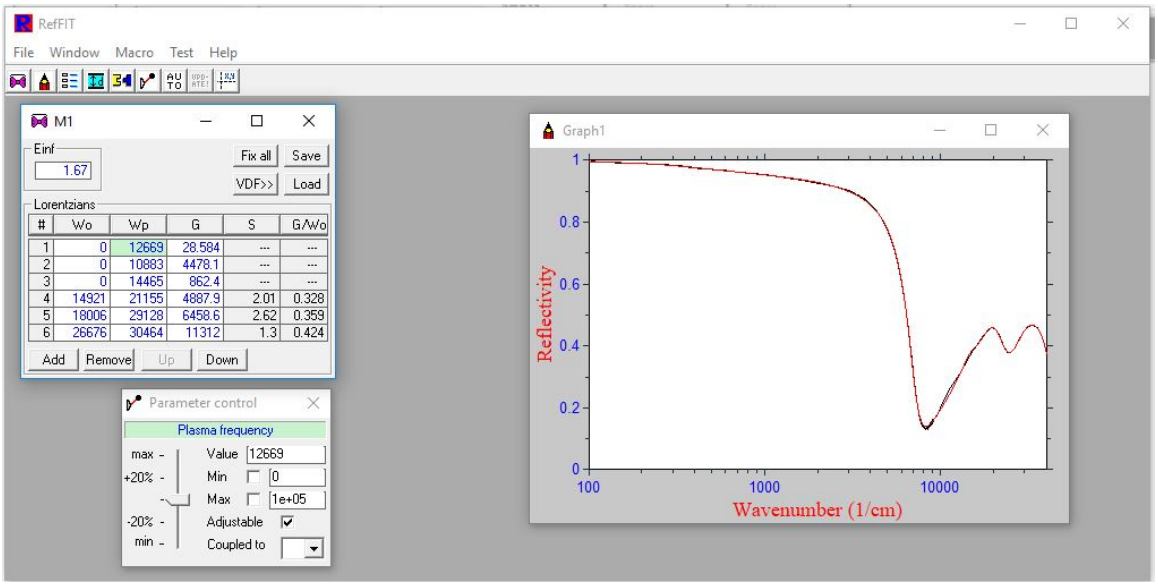

Figure 4.10: Well fitted curve using three Drude and three Lorentz modes.

There is another important feature of RefFit program, and it's called "automated fitting tool". One can use this feature to fit graphs automatically. First, choose "Fit" from the window menu, add the desired dataset and model from the "Add" button, and click "START". Although this feature gives the best fitting curve, some-

times the values may be out of range. Therefore it's better to fix the known (fixed) parameters by right clicking the mouse on the parameter and modifying it. Once you have fixed the parameters in the model, they display in red instead of the normal blue color.

After getting the best fitting curve, you can save or export the fitted data to a text file. To export, choose the fitted graph and then press "space bar" which opens a window to give the file name and location to be saved.

CHAPTER V

EXPERIMENTAL DATA

In this study, the main target was to study the optical properties of the quasi-two-dimensional dichalcogenides 2H-$TaSe_2$ and 2H-$NbSe_2$ in an attempt to address the physics of two-dimensional correlated systems. Measurements with linearly polarized light give both the in-plane(ab-plane) and out-of-plane(c-axis) components of the conductivity tensor. The layered crystal structure suggests strong anisotropy between in-plane(ab-plane) and inter-plane(c-axis) response. For this analysis, four temperatures for $NbSe_2$ and three temperatures for $TaSe_2$ were modeled from experimental data.

Table 5.1: Temperatures of four data sets

$NbSe_2$		$TaSe_2$	
ab-plane	c-axis	ab-plane	c-axis
10 K	10 K	20 K	6 K
35 K	35 K		
80 K	80 K	100 K	100 K
295 K	300 K	300 K	300 K

Using the RefFit software this data was plotted. These data especially about the reflectivity of these materials with the frequency.

5.1 Reflectance of Metals

The optical responses of metals mainly originates from conduction electrons. Metals have high reflectivity at almost all wavelengths in the visible region and infrared region of the spectrum. As previously discussed, the Drude model of free electrons states that the electrons in a metal behave like classical gas molecules[26].

It is important to know about the reflectance of metals to compare that data with our data. The reflection of gold and aluminum is given in figure 5.1. This data can be compared with our data in the infrared region. For metals, the plasma edge occurs at very high frequencies; our data's plasma edge occurs below frequency 10000 cm^{-1}. The plasma edge for gold and aluminum, however, are around 20000 cm^{-1} and 60000 cm^{-1} respectively.

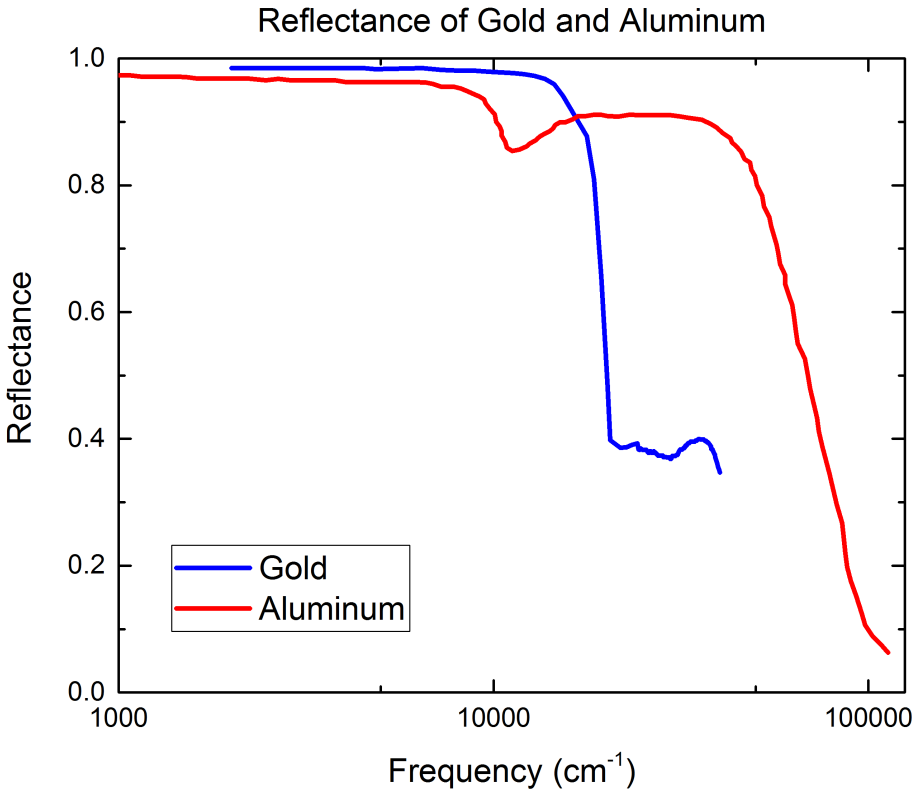

Figure 5.1: Reflectance of gold (Frquency range 2000 - 40000 cm^{-1}) and aluminum (Frequency range 800 - 113000 cm^{-1}) as functions of log frequency[1].

5.2 $NbSe_2$ data

5.2.1 *ab*-plane (in-plane) data

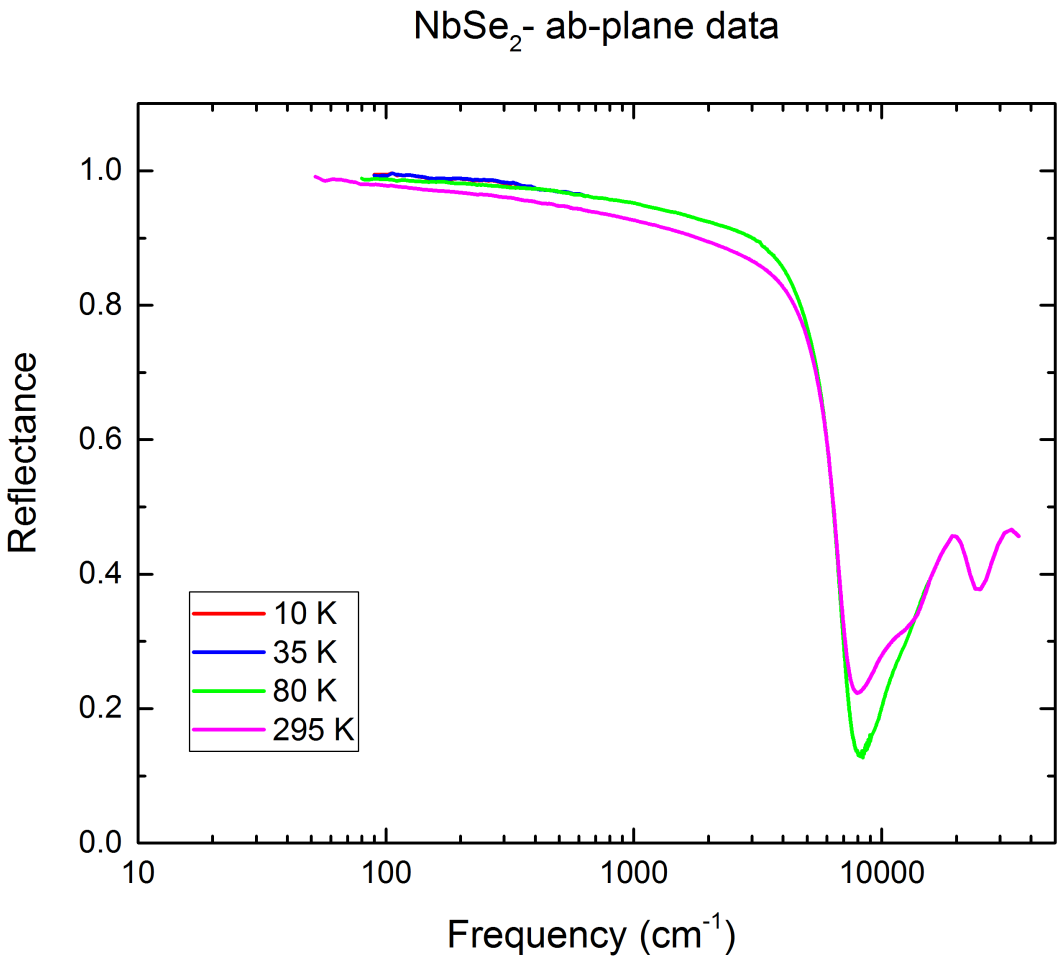

Figure 5.2: *ab*-plane data at the temperatures 10 K, 35 K, 80 K, and 295 K.

Reflectance data were fitted using Origin software, the y-axis is a linear scale indicating reflectance, and the x-axis is a log scale indicating frequency. Figure 5.2 shows the data of $NbSe_2$ for *ab*-plane. All the data in low temperatures are very

similar, but there are some slight differences. But, for 295 K, there is a significant difference of in curve. The reflectivity is decreasing with increasing frequency at low frequencies.

The reflectance depends on the electronic structure of 2H-$NbSe_2$. In normal conditions, the electrons in the conduction band is lower than the electrons in the valance band. Therefore, the collisions of electrons are less within the materials. When the electrons in the valence band receive more energy with the increase of temperature, thus they are excited and jump to the conduction band and the number of collisions increases. Therefore, the reflectance of the material reduces.

In this work, data for four temperatures was taken. Reflectivity decreases as temperature increases. When temperature increases, the materials absorb the temperature and the electrons are excited. Therefore, the number of electron collisions increase.

5.2.2 *c*-axis (inter-plane) data

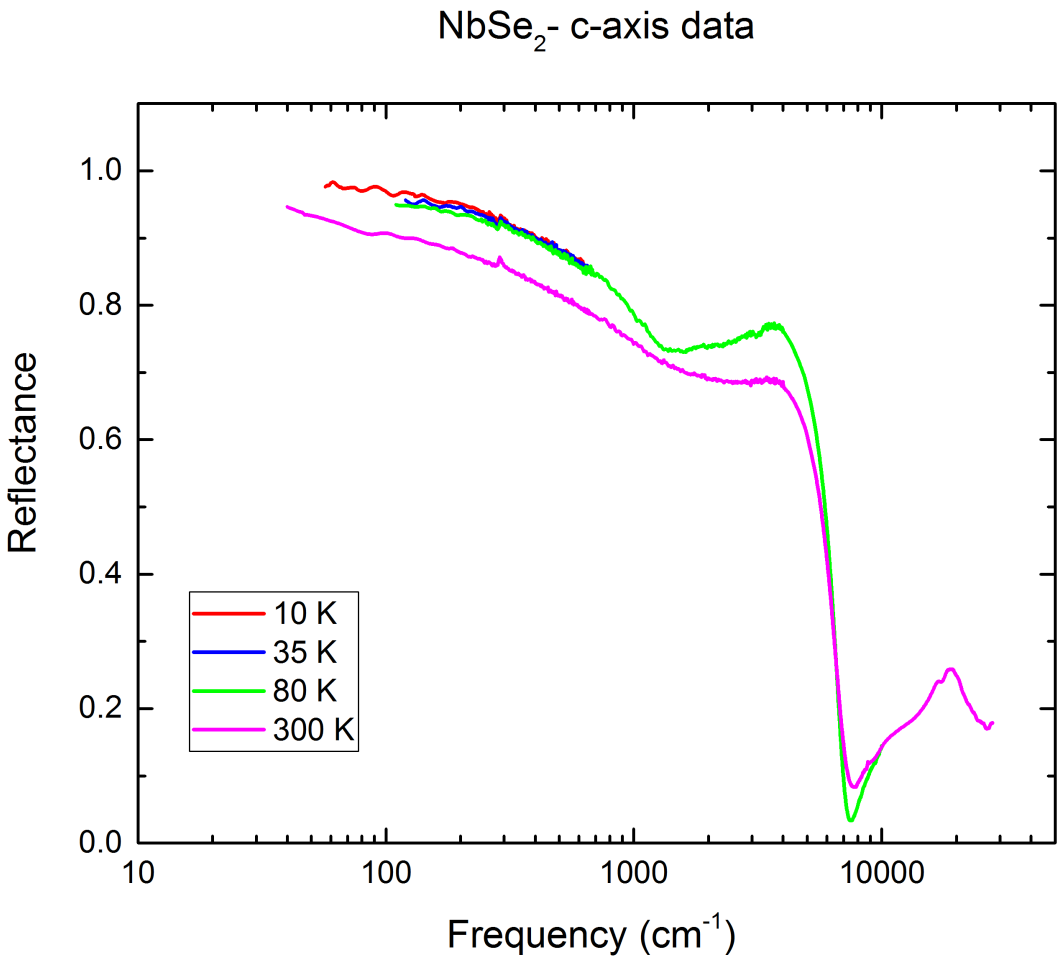

Figure 5.3: *c*-axis data at the temperatures 10 K, 35 K, 80 K, and 300 K.

The *c*-axis data is shown in figure 5.3. For very low frequencies, the reflectivity decreases with increasing temperature. But, around the plasma edge, the reflectivity decreases as temperature increases because the Lorentz peaks are getting narrower.

When discussing the c-axis, the reflectivity is less than in the ab-plane because the mean free path for an electron is less than the lattice point distances. Therefore, the collisions are higher along c-axis than the ab-plane.

5.3 $TaSe_2$ data

5.3.1 *ab*-plane (in-plane) data

Reflectance of $TaSe_2$ for *ab*-plane and *c*-axis are shown in figure 5.4 and 5.5 respectively. These data also have the same behavior. They are really distinguishable for low frequencies than that of the $NbSe_2$, but after plasma frequency all the data are same.

$TaSe_2$ also has conduction electrons in conduction band and valence electrons in valence band. For low frequencies (less than plasma edge) the reflectivity is high due to the less number of electron collision. As increase the frequency, the number of collisions increase (interband trnsition occur at this point) in ab-plane and causes for low reflectivity. The frequency dependance of 2H-$TaSe_2$ is easily understandable by looking at these data.

In the frequency range from far infrared to UV, the reflectivity goes down as increase the temperature of the material. From the plasma edge the data is same for all temperatures, because after the plasma edge the maximum number of collisions remain same for 2H-$TaSe_2$. When temperature decreases, the reflectance increases at low frequencies (roughly before the plasma edge). Reflectance decreases around plama frequencies when we increase the temperature because the Lorentz peaks are getting narrower.

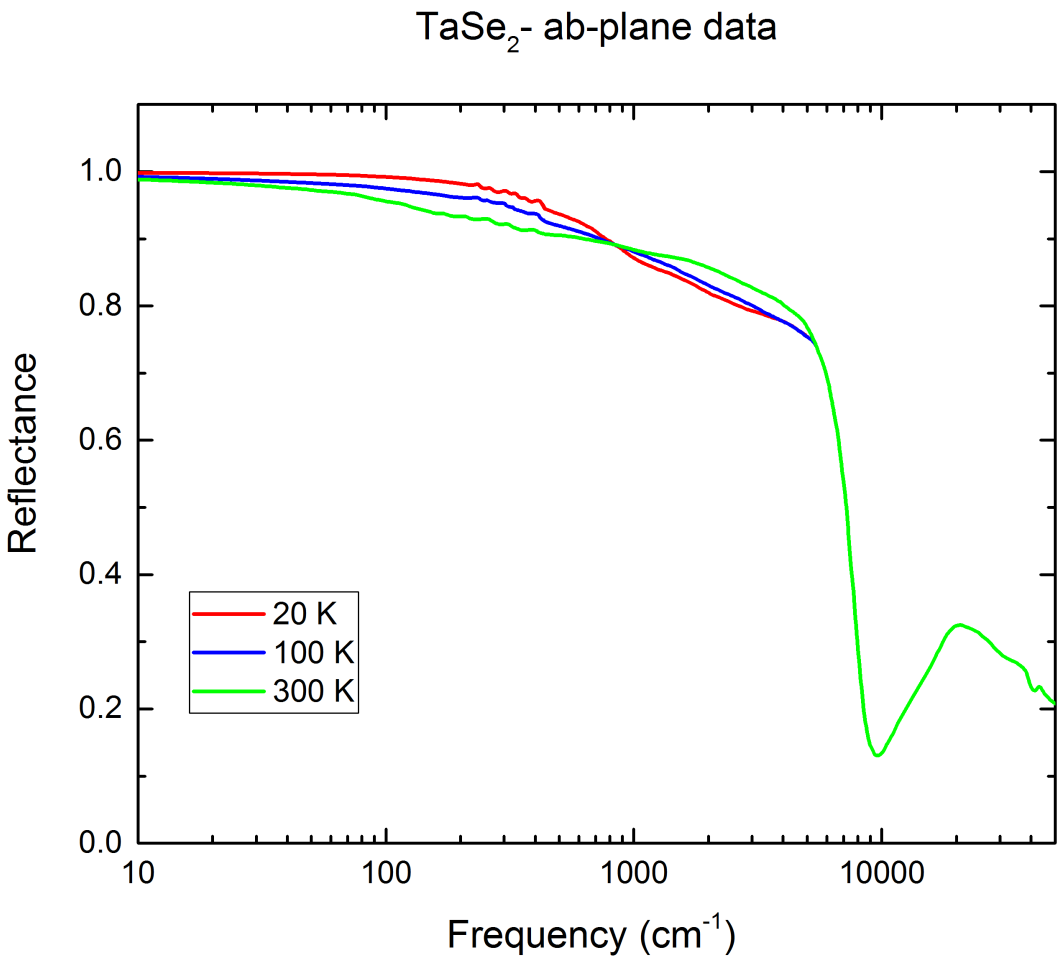

Figure 5.4: *ab*-axis data at the temperatures 20 K, 100 K, and 300 K.

5.3.2 c-axis (inter-plane) data

As $TaSe_2$ is also a layered material, the distance (along c-axis) between two layers is smaller than the lattice spacing in the ab-plane. Therefore, more collisions occur along the c-axis than in the ab-plane, where the mean free path is larger. Then, the reflectivity for the c-axis is lower than the reflectivity in the ab-plane.

The reflectivity decreases as the frequency and temperature increase. When the temperature increases, the reflectance decreases and when the temperature decreases, the reflectance increases. Plama edge can be roughly described as the border of the high reflectance and the low reflectance of the material. Frequency and the temperature variations can be easily identified from the graph. Further details about the fitted graphs are given in chapter 6.

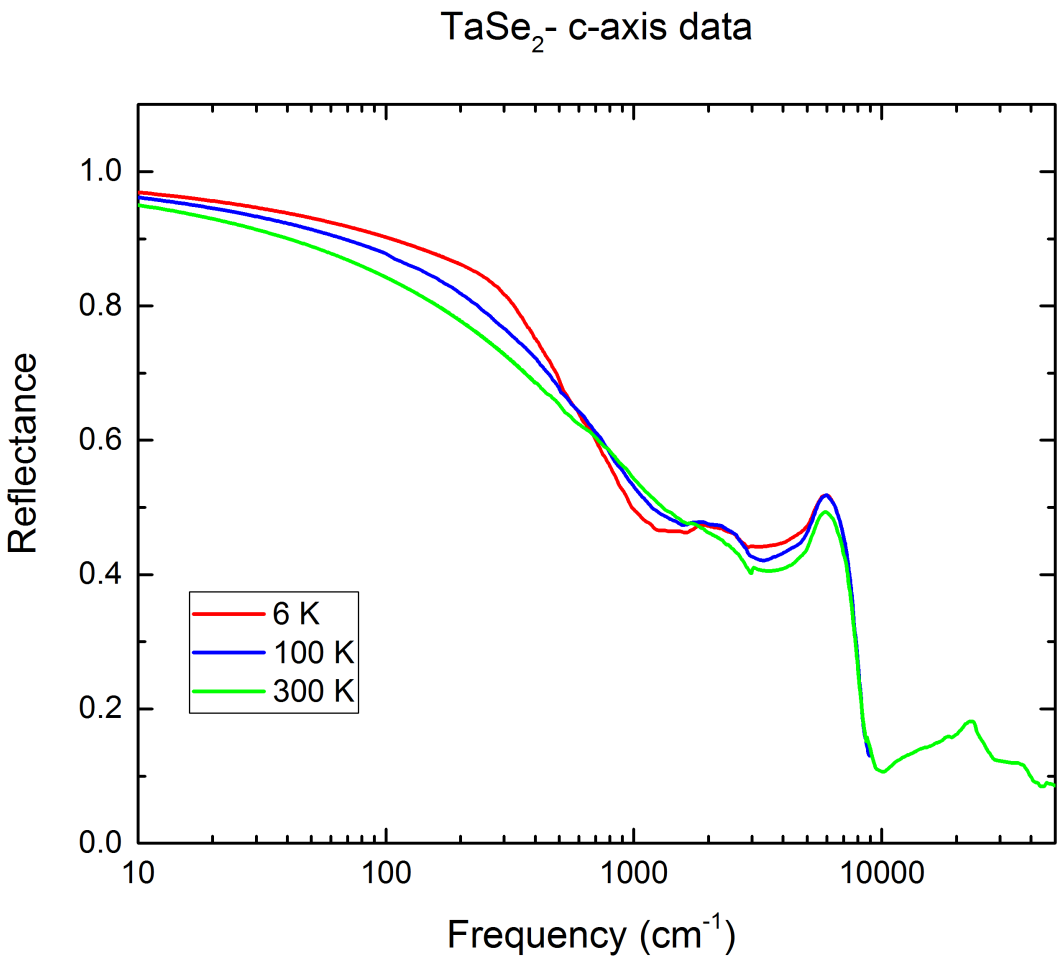

Figure 5.5: *c*-axis data at the temperatures 6 K, 100 K, and 300 K.

CHAPTER VI

RESULTS AND DISCUSSION

This chapter will present the analyzed optical data of the material 2H-$NbSe_2$ and 2H-$TaSe_2$. Here, we analyzed the reflectance data in the ab-plane(in-plane) and c-axis(inter-plane) of these materials for different temperatures. This data was collected using FTIR and UV-visible optical measurements. In particular, the reflectance data was analyzed. The results were fitted and analyzed using RefFit and graphs were generated by using the graphing software Origin. For the graphs, reflectance is set in the y-axis and frequency (wavenumber) is set in the x-axis. Reflectivity measurements of 2H-$TaSe_2$ and 2H-$NbSe_2$ were performed over a frequency range of 20 to 130000 cm^{-1} and 40 - 50000 cm^{-1}, respectively, on mechanically polished samples. Therefore x-axis is displayed in log scale.

6.1 Reflectance data

In Figure 6.1, we see all data for the ab-plane and c-axis of the two materials across the noted frequency ranges.

To compare easily, the reflectance data was plotted in the frequency range of 10 - 50000 cm^{-1}. The two materials exhibit similar changes in reflectance with respect to frequency. The reflectance of ab-plane of both materials slightly decrease

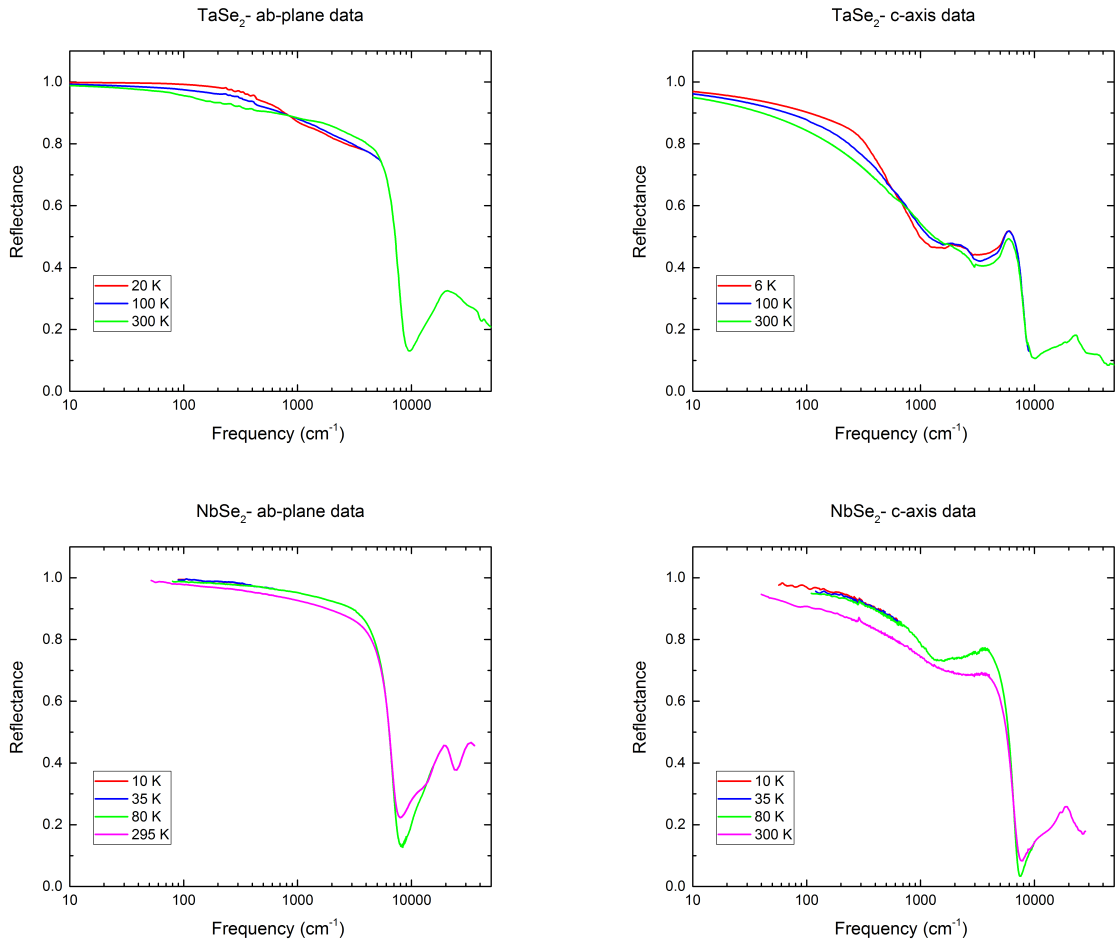

Figure 6.1: Reflectivity data for $TaSe_2$ and $NbSe_2$.

from low frequencies until around 5000 cm^{-1}. After that, the reflectance decreases drastically down to 7000 cm^{-1}, after which the reflectance increases gradually up to 20000 cm^{-1} before again decreasing. The c-axis reflectance data of both materials decrease gradually down to 2000 cm^{-1} and then increase and again decrease drastically down to 7000 cm^{-1}.

As noted earlier about the reflectance of metals, our data behaves similarly

to the reflectance of metals. But, for these materials, the plasma edge is very low, occurring below 10000 cm^{-1}. Reflection before the plasma edge frequency is due to the conduction electrons of the material; after the plasma edge, the reflection is due to the interband transition.

If we look at the data carefully, we can see that the interband transition is similar for every temperatures of $TaSe_2$ for both the *ab*-plane and *c*-axis. But, if we consider $NbSe_2$, the interband transition is slightly different for higher temperatures and lower temperatures for both the *ab*-plane and *c*-axis. Before the plasma edge frequency, we can say the conduction electrons differ with respect to temperature.

When we consider *c*-axis data for both materials, they also have similar behavior; the reflectance decreases for a certain frequency range and then increases up to the plasma frequency. However, the plasma frequency is different for both materials, being 7000 cm^{-1} for $TaSe_2$ and 6000 cm^{-1} for $NbSe_2$.

6.2 Resulted Fits

6.2.1 $NbSe_2$

$NbSe_2$ *ab*-plane

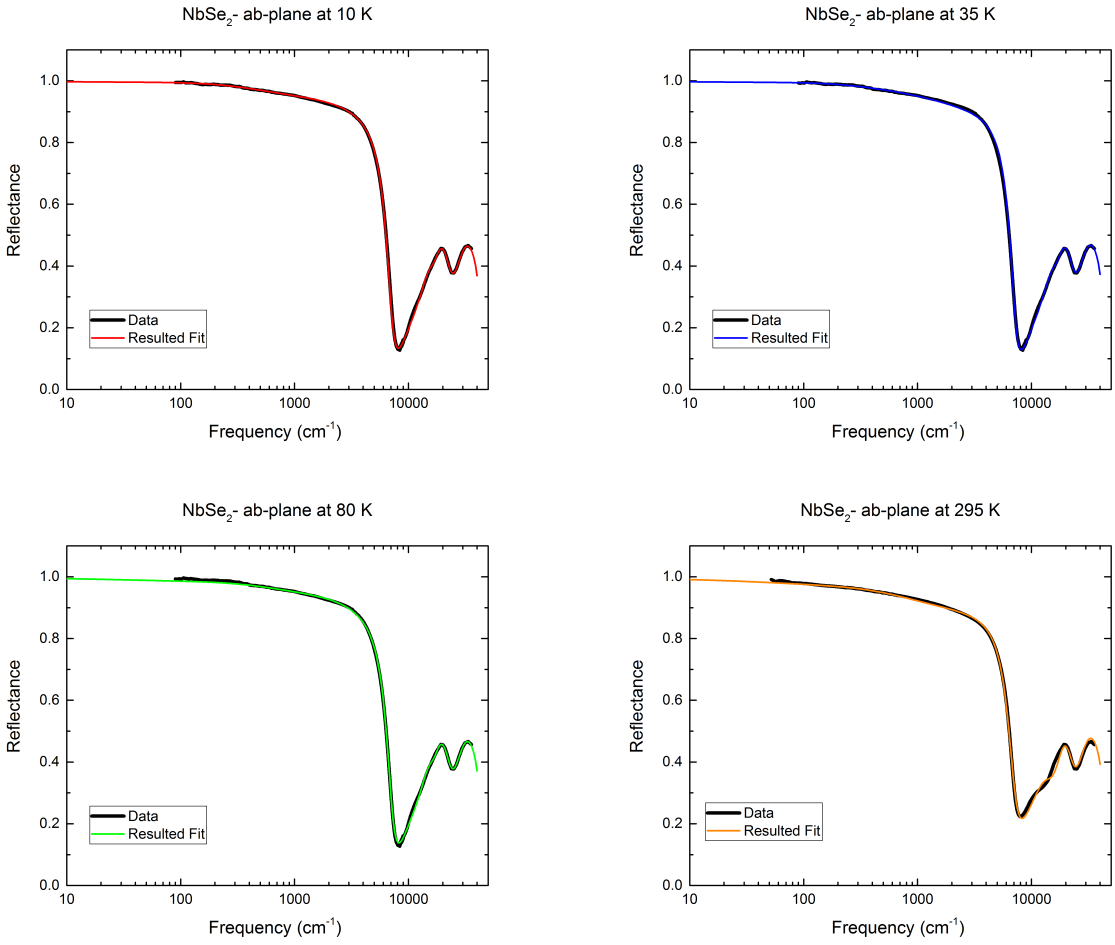

Figure 6.2: Individual fits for the *ab*-plane of $NbSe_2$ at temperatures 10 K, 35 K, 80 K, and 295 K.

As described earlier, the combination of the Drude and Lorentz models can be used to describe intraband and interband electronic transitions. In this study, the reflectance data was modeled using the RefFIT program as discussed in chapter 3. Each Lorentzian has three parameters-transverse frequency ω_0, plasma frequency ω_P, and scattering rate γ-that can be adjustable during the fit. When the transverse frequency ω_0 is zero and other parameters have values, it is considered as a Drude model; otherwise, the fit is considered a Lorentz model.

$NbSe_2$ - *ab*-plane resulted reflectance fits are shown in figure 6.3. The fitting parameters are given in the table 6.1 . The plasma edge is around 6000 cm^{-1} for all temperatures. The reflectance is in the range of 0.8 - 1.0 for low frequencies. The reflectance is temperature dependent. According to the experiment data, for these low frequencies, reflectance increases when temperature decreases. But, after the plasma edge frequency, the reflectance is almost the same for all temperatures. Therefore, we can say reflectance depends on the temperature exclusively when frequency is low.

Since simpler fits reduce analysis difficulty, the first attempt at fitting the experimental data used only one Drude and one Lorentz mode. Unfortunately, it proved difficult to accurately fit the data with so few for both materials.

For the *ab*-plane $NbSe_2$ data,three Drude and three Lorentz fits proved necessary. They are displayed in figure 6.3 with the parameters of table 6.1.

Table 6.1: $NbSe_2$ *ab*-plane fitting parameters for four temperatures. (a) for 10 K, (b) for 35 K, (c) for 80 K, and (d) for 295 K.

ω_0	ω_P	γ	ω_0	ω_P	γ
0	12669	28.58	0	12720	31.08
0	10301	4119.9	0	10490	4200
0	14465	862.4	0	14112	900
14921	21155	4887.9	14921	21155	4887.9
18006	29128	6458.6	18006	29128	6458.6
26676	30464	11312	26676	30464	11312
(a)			(b)		
ω_0	ω_P	γ	ω_0	ω_P	γ
0	13732	105.7	0	19979	1750.8
0	10832	4493.5	0	11928	200.64
0	13501	925.85	13116	23211	7304.1
14921	21155	4887.9	18006	29128	6458.6
18006	29128	6458.6	26676	30464	11312
26676	30464	11312			
(c)			(d)		

$NbSe_2$ c-axis

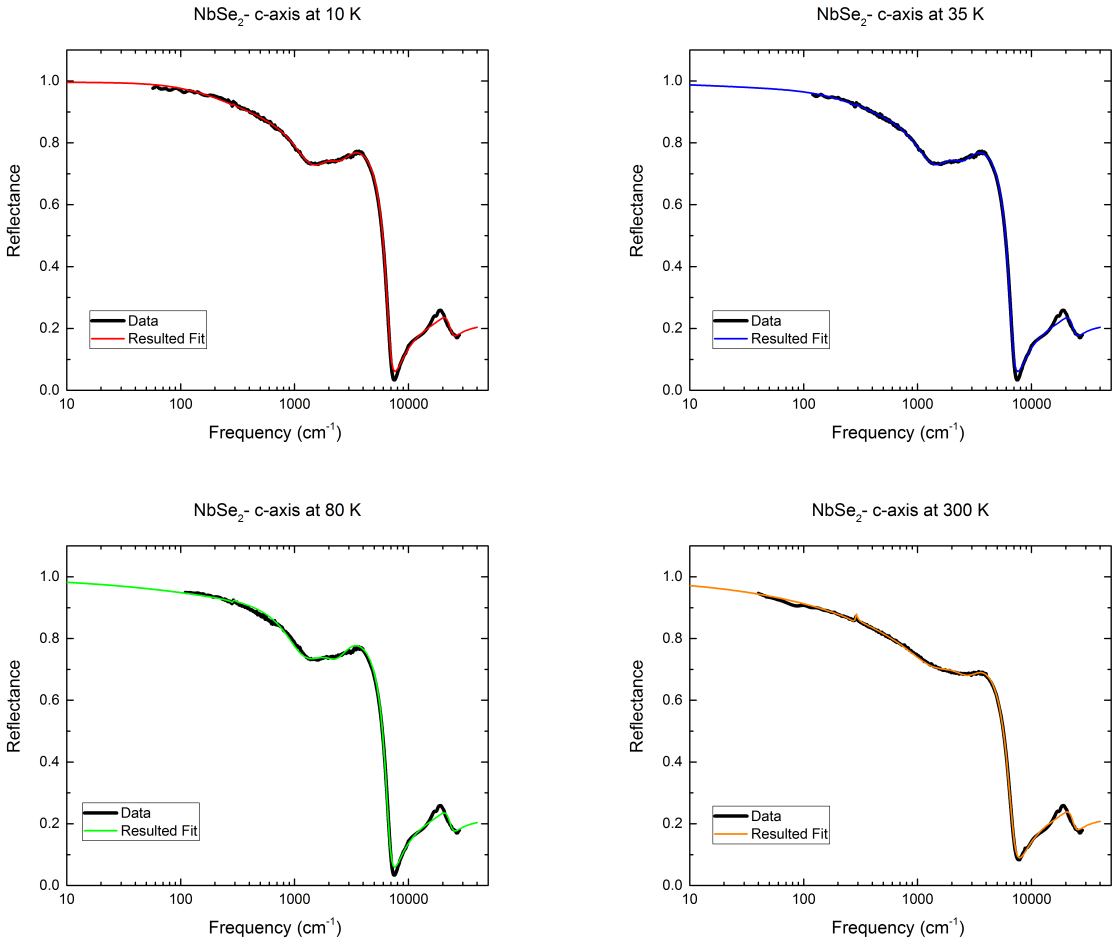

Figure 6.3: Individual resulted fits for c-axis of $NbSe_2$ at temperatures 10 K, 35 K, 80 K, and 300K.

The resulted reflectance fits of $NbSe_2$ along c-axis is shown in figure 6.4. We can see distinguishable fitting curves for different temperatures in the region below 6000 cm^{-1}. It is also same as the ab-plane, reflectance decreases when the temperature increases. But the reflectance after the plasma edge is almost same. The fitting parameters are given in the table 6.2. For c-axis two Drude models and four Lorentz models were used to get a better fitting curves.

Table 6.2: $NbSe_2$ c-axis fitting parameters for four temperatures. (a) for 10 K, (b) for 35 K, (c) for 80 K, and (d) for 300 K.

ω_0	ω_P	γ	ω_0	ω_P	γ
0	11900	1048.7	0	11610	1101.6
0	4488.5	10.2	0	4596.8	67.68
287.01	250.18	2.10	287.7	337.26	4.36
1853	9796.2	1342.1	1815	9809.8	1299.5
2760.6	10200	1751.6	2756.5	10282	1743
22439	17758	5560.2	22439	17758	5560.2
(a)			(b)		
ω_0	ω_P	γ	ω_0	ω_P	γ
0	9109.5	1387.4	0	5407.5	1589.8
0	7800.7	338.91	0	11056	1585.4
289.7	474.71	8.8517	285.79	576.9	9.14
1690.7	10000	1403.6	1922	10141	1890.5
2643.1	10656	1580.2	3135.4	10719	2188.6
22439	17758	5560.2	22439	17758	5560.2
(c)			(d)		

6.2.2 $TaSe_2$

$TaSe_2$ *ab*-plane

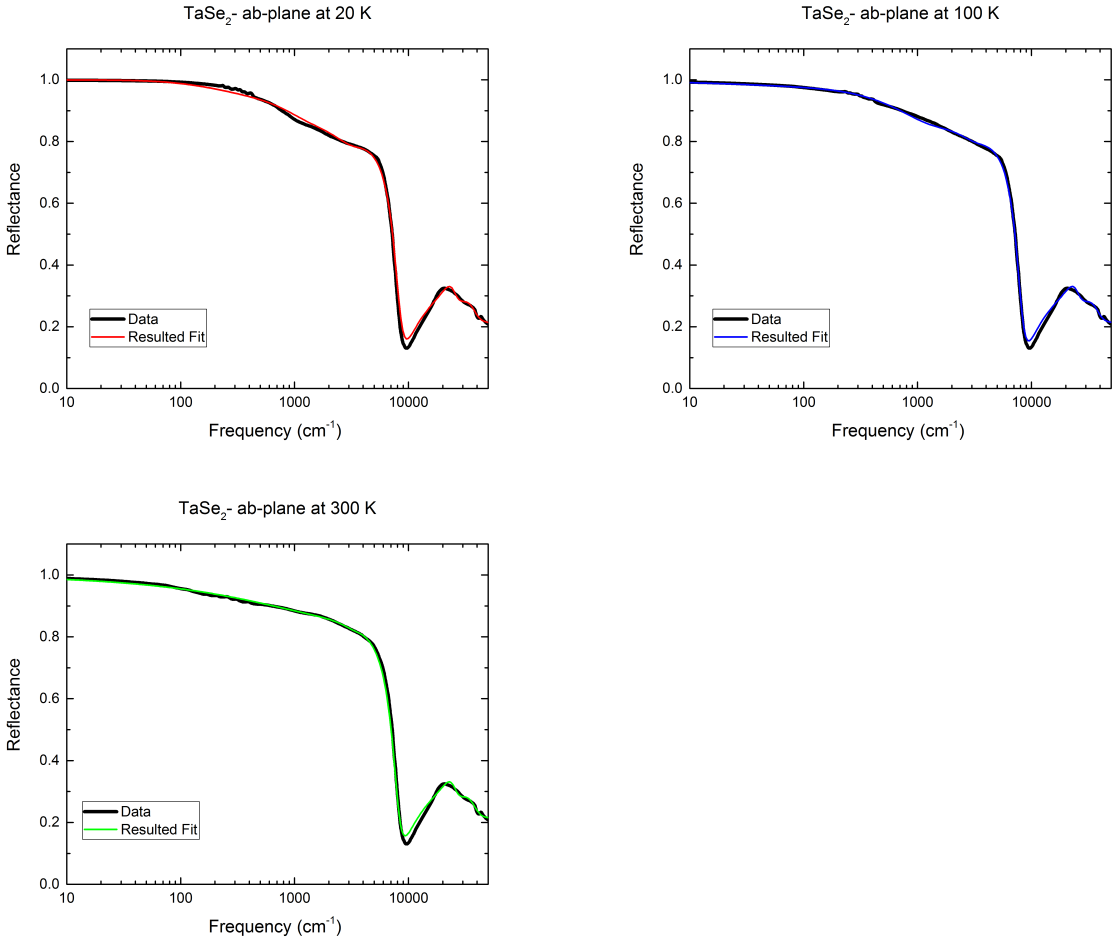

Figure 6.4: Individual resulted fits for *ab*-plane of $TaSe_2$ at temperatures 20 K, 100 K, and 300 K.

The reflectance curves for ab-plane of $TaSe_2$ are similar to the resulted reflectance curves for ab-plane of $NbSe_2$. Plasma edge occurs around 7000 cm^{-1}. Although curves can be distinguishable before the plasma edge frequency, they are almost similar after the plasma edge. Below 1000 cm^{-1} frequency, the reflectance increases when the temperature decreases. Parameters are given in table 6.3. To get better fits for ab-plane data of $TaSe_2$, two Drude and five Lorentz modes had been used.

Table 6.3: $TaSe_2$ *ab*-plane fitting parameters for three temperatures. (a) for 20 K, (b) for 100 K, and (c) for 300 K

ω_0	ω_P	γ
0	15311	682.21
0	7573.9	0.8576
1637.7	19612	2969.4
3445.7	12830	3044.7
24074	30376	8300.6
34894	45760	17566
67835	112334.41	62525

(a)

ω_0	ω_P	γ
0	15409	1004.7
0	8497	117.76
1637.7	18687	2535.2
3445.7	11973	3061.4
24074	30376	8300.6
34894	45760	17566
67835	112334.41	62525

(b)

ω_0	ω_P	γ
0	15600	1973.1
0	22800	2158.7
1637.7	5500	2808.7
3445.7	4289.4	1715.2
24074	30376	8300.6
34894	45760	17566
67835	112334.41	62525

(c)

$TaSe_2$ c-axis

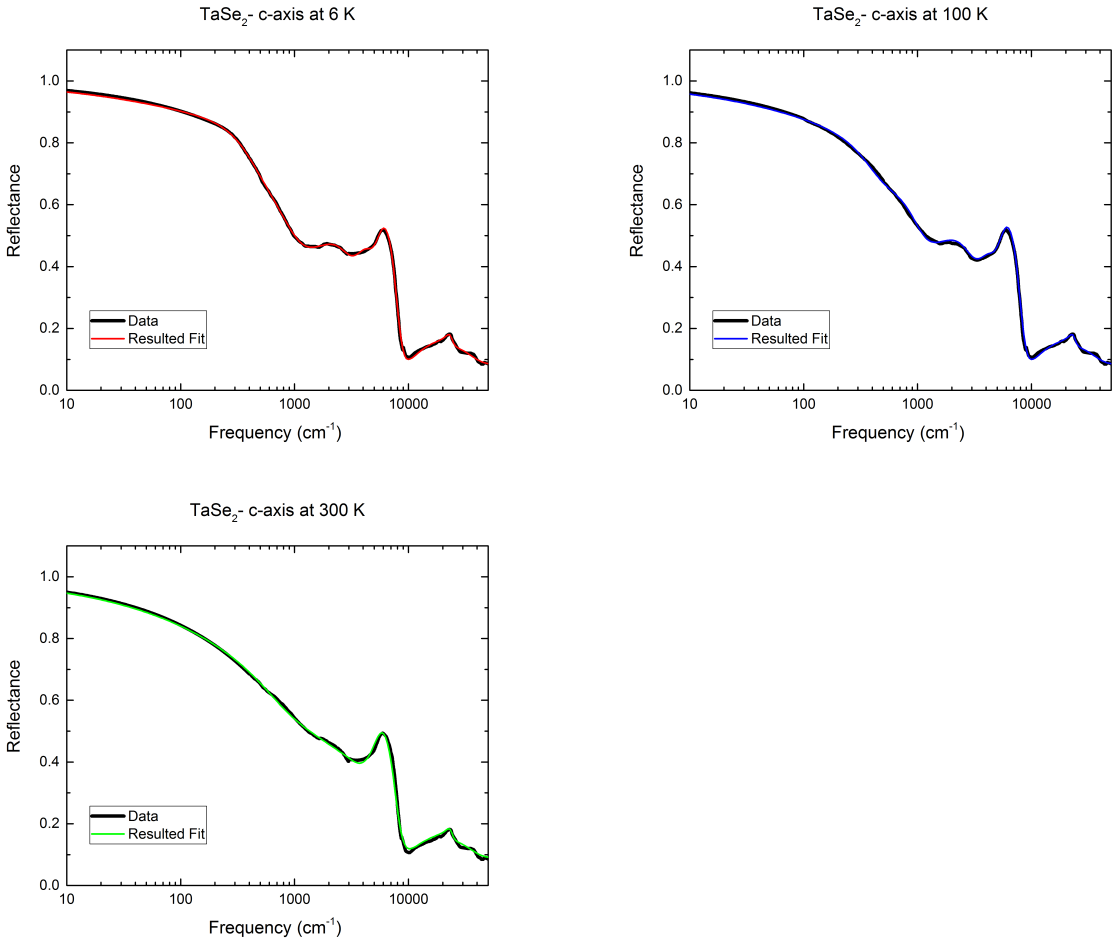

Figure 6.5: Individual resulted fits for c-axis of $TaSe_2$ at temperatures 6 K, 100 K, and 300 K.

We were able get better fitting curves for c-axis data of $TaSe_2$ using one Drude model and six Lorentz modes. This result indicates that reflectance occurs mainly due to the interband trasition of these materials.

Table 6.4: $TaSe_2$ c-axis fitting parameters for three temperatures. (a) for 6 K, (b) for 100 K, and (c) for 300 K.

ω_0	ω_P	γ
0	3706.8	232.55
728.71	4178.2	1288.4
2436.2	8323.4	2300.1
4214.6	8787.1	2088.2
5607.3	11673	2014.2
23347	9810.6	3795.9
32984	48793	41790

(a)

ω_0	ω_P	γ
0	3786.4	347.25
732.79	3841.5	913.09
2348.5	8774.1	2275.5
4208.5	7742.7	2081.3
5597.4	12307	2034.1
23347	9810.6	3795.9
32984	48793	41790

(b)

ω_0	ω_P	γ
0	4977.1	919.18
306.79	670.06	1149.4
2337.4	10779	5063.5
3161	5063.9	3159.6
5473.3	12744	2200
23347	9810.6	3795.9
32984	48793	41790

(c)

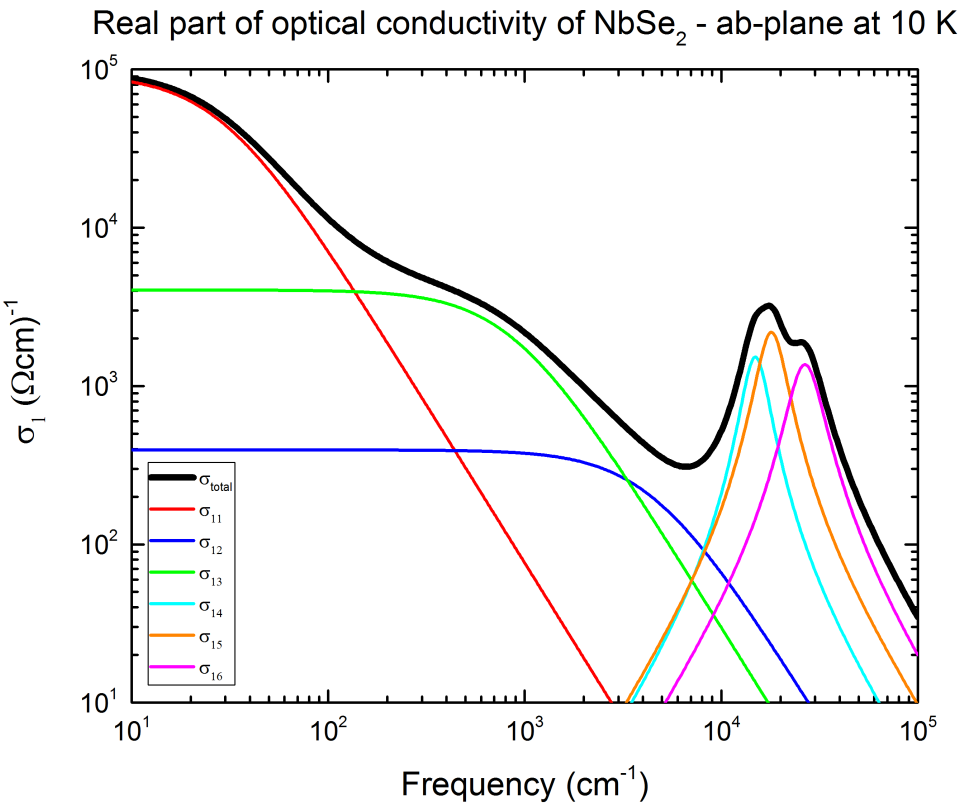

Figure 6.6: Total and individual components of the real part of optical conductivity (σ_1) as a function of frequency (cm^{-1}) for $NbSe_2$ *ab*-plane at temperature 10 K.

Measuring Optical conductivity (σ) is one of the main methods used to understanding the optical properties of a materials. Optical conductivity directly depends on the refractive index (n) and the absorption coefficient (α) of a material. It consists of a real part and imaginary part, σ_1 and σ_2, respectively. Here we consider the real part of the conductivity only.

Table 6.5: Fitting parameters of $NbSe_2$ *ab*-plane at 10 K.

Mode	ω_0	ω_P	γ
1	0	12669	28.58
2	0	10301	4478.1
3	0	14465	862.4
4	14921	21155	4887.9
5	18006	29128	6458.6
6	26676	30464	11312

Figure 6.6 shows the total and individual components of the real part of the optical conductivity of $NbSe_2$ *ab*-plane at 10 K. We mentioned previously that we had to use six individual modes to construct a better fit for the reflectance data. We have used three Drude modes (σ_{11}, σ_{12}, σ_{13}) to represent the conductivity due to conduction electrons and three Lorentz modes (σ_{14}, σ_{15}, σ_{16}) to represent the conductivity due to interband transition as shown in figure 6.6. The fitting parameters are given in table 6.4. The black curve represents the real part of the total optical conductivity while the colored curves represent the individual modes. Model (S_1) in RefFIT was used to construct the plot. Both the real part of the optical conductivity and the frequency were plotted in log scale. High optical conductivities can be seen at low frequencies. It then decreases with frequency down to 7000 cm^{-1}, followed by a peak at 20000 cm^{-1} and another decease.

Here we have given only one graph at 10 K. But, for the other temperatures (35 K and 80 K), the last three Lorentz modes are the same. For 295 K, the last two Lorentz modes are the same. Optical conductivity of the material is changed with the temperature due to the changing of Drude modes. This means that interband transition doesn't change the optical conductivity of the material whereas conduction electrons do.

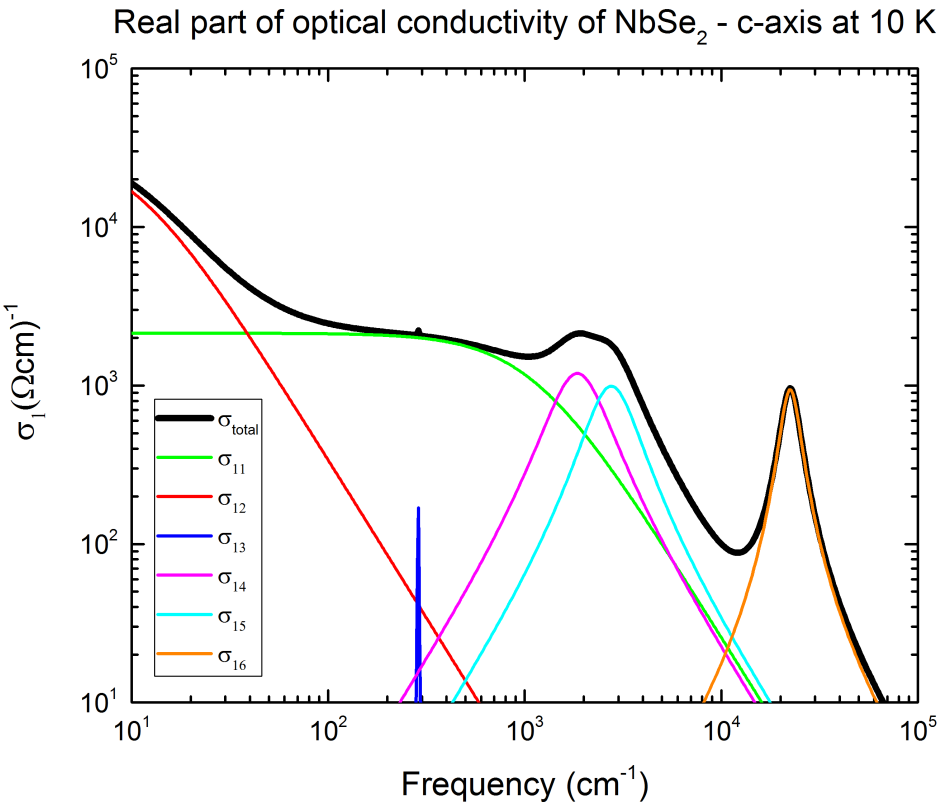

Figure 6.7: Total and individual components of the real part of optical conductivity (σ_1) as a function of frequency (cm^{-1}) for $NbSe_2$ c-axis at temperature 10 K.

Figure 6.7 shows the total and individual components of the real part of optical conductivity of the $NbSe_2$ c-axis at temperature 10 K. Here we have used two Drude modes and four Lorentz modes. As in the ab-plane, higher reflectance can be seen at low frequencies. σ_{13} represents phonon and its contribution to the total curve is less.

Table 6.6: Fitting parameters of $NbSe_2$ c-axis at 10 K.

Mode	ω_0	ω_P	γ
1	0	11900	1103.9
2	0	4488.5	10.2
3	287.01	250.18	2.10
4	1853	9796.2	1342.1
5	2760.6	10200	1751.6
6	22439	17758	5560.2

The fitting parameters of figure 6.7 are given in table 6.5. ω_P is 250.18 for the phonon. A broad peak and a narrow peak are in the plot at 3000 cm^{-1} and 25000 cm^{-1} respectively. The broad peak is unusual, so we had to use two Lorentz modes to get a better fit. The axes were kept the same in all graphs to compare the optical conductivity of ab-plane and c-axis easily. If we compare the conductivity of ab-palne and c-axis of $NbSe_2$, the optical conductivity in the ab-plane is higher than the optical conductivity of the c-axis.

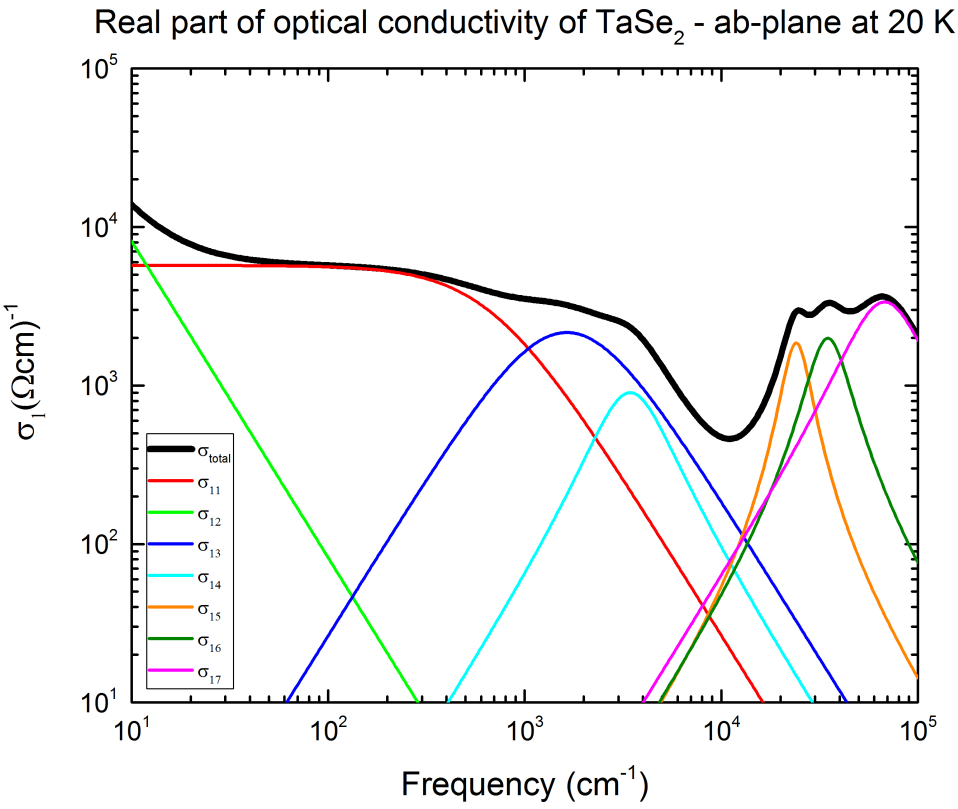

Figure 6.8: Total and individual components of the real part of optical conductivity (σ_1) as a function of frequency (cm^{-1}) for $TaSe_2$ *ab*-plane at temperature 20 K.

The real part of the total conductivity and individual modes for $TaSe_2$ *ab*-plane at temperature 20 K are shown in Figure 6.8. We had to use two Drude modes and five Lorentz modes to get a good fit. The conductivity of the $TaSe_2$ *ab*-plane is less than the conductivity of $NbSe_2$ *ab*-plane at low frequencies, but the decrement of the conductivity with the frequency is less when compared to the decrement of $NbSe_2$.

Table 6.7: Fitting parameters of $TaSe_2$ *ab*-plane at 20 K.

Mode	ω_0	ω_P	γ
1	0	15311	682.21
2	0	7573.9	0.8576
3	1637.7	19612	2969.4
4	3448.7	12830	3044.7
5	24074	30376	8300.6
6	34894	45760	17566
7	67835	112334.41	62525

Table 6.7 gives the relevant parameters to each individual modes.

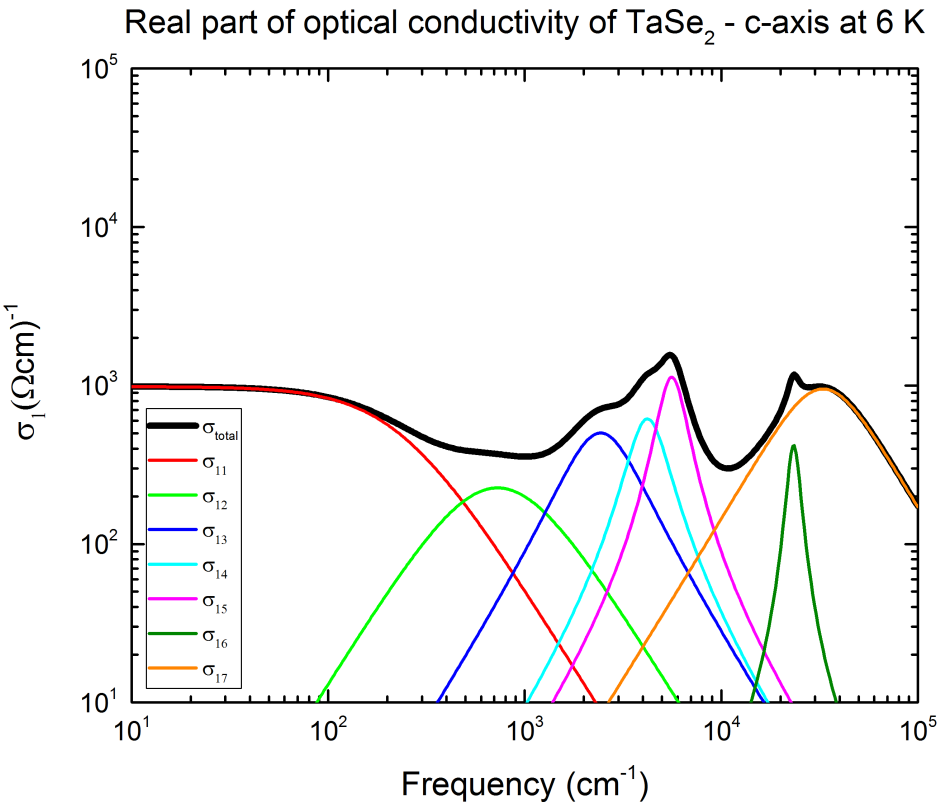

Figure 6.9: Total and individual components of the real part of optical conductivity (σ_1) as a function of frequency (cm^{-1}) for $TaSe_2$ c-axis at temperature 6 K.

Real part of the total optical conductivity and the individual modes are shown in figure 6.9. One Drude and six Lorentz modes were used to get a better fit. At low frequencies, the conductivity is low when compared to $TaSe_2$ ab-plane, $NbSe_2$ ab-plane and c-axis curves. The maximum conductivity is about 6000 cm^{-1} after which a sudden decease in the conductivity occurs around 10000 cm^{-1}, the plasma frequency. The fitting parameters are given in table 6.8.

Table 6.8: Fitting parameters of $TaSe_2$ c-axis at 6 K.

Mode	ω_0	ω_P	γ
1	0	3706.8	232.55
2	728.71	4178.2	1288.4
3	2436.2	8323.4	2300.1
4	4214.6	8787.1	2088.2
5	5607.3	11673	2014.2
6	23347	9810.6	13795.9
7	32984	48793	41790

6.4 Comparison of the optical conductivity (σ) between ab-plane and c-axis of two materials

If we consider the real part of the optical conductivity of both material's ab-plane, the conductivity of $NbSe_2$ is higher than the conductivity of $TaSe_2$ at similar temperatures. To model the conductivity of $NbSe_2$, we had to use three Drude modes before the plasma edge and three Lorentz modes after the plasma edge. But for the $TaSe_2$, two Drude and two Lorentz modes have been used to get the conductivity before the plasma edge while three Lorentz modes after the plasma edge. Both materials show metallic behavior for ab-plane.

Two Drude, four Lorentz modes and one Drude, six Lorentz modes were used to construct the conductivity of $NbSe_2$ and $TaSe_2$, respectively. The conductivity is higher for the c-axis of $NbSe_2$ that of $TaSe_2$. A special thing, a phonon can be seen in $NbSe_2$ c-axis. These data were taken at 10 K and 6 K for $NbSe_2$ and $TaSe_2$, respectively. These temperatures can be considered as similar.

If we compare the conductivity data of ab-plane and c-axis within a same material, we could see the conductivity of c-axis is less than that of the ab-plane in both materials. Because conduction electrons are more dominant in the ab-plane and that results the higher conductivity in ab-plane.

6.5 Temperature dependence of fitting parameters

In this section we will discuss the temperature dependence of the fitting parameters, plasma frequency and scattering rate. Figure 6.10 and figure 6.11 show plasma frequency (ω_P) and scattering rate (γ) as a fuction of temperature, respectively.

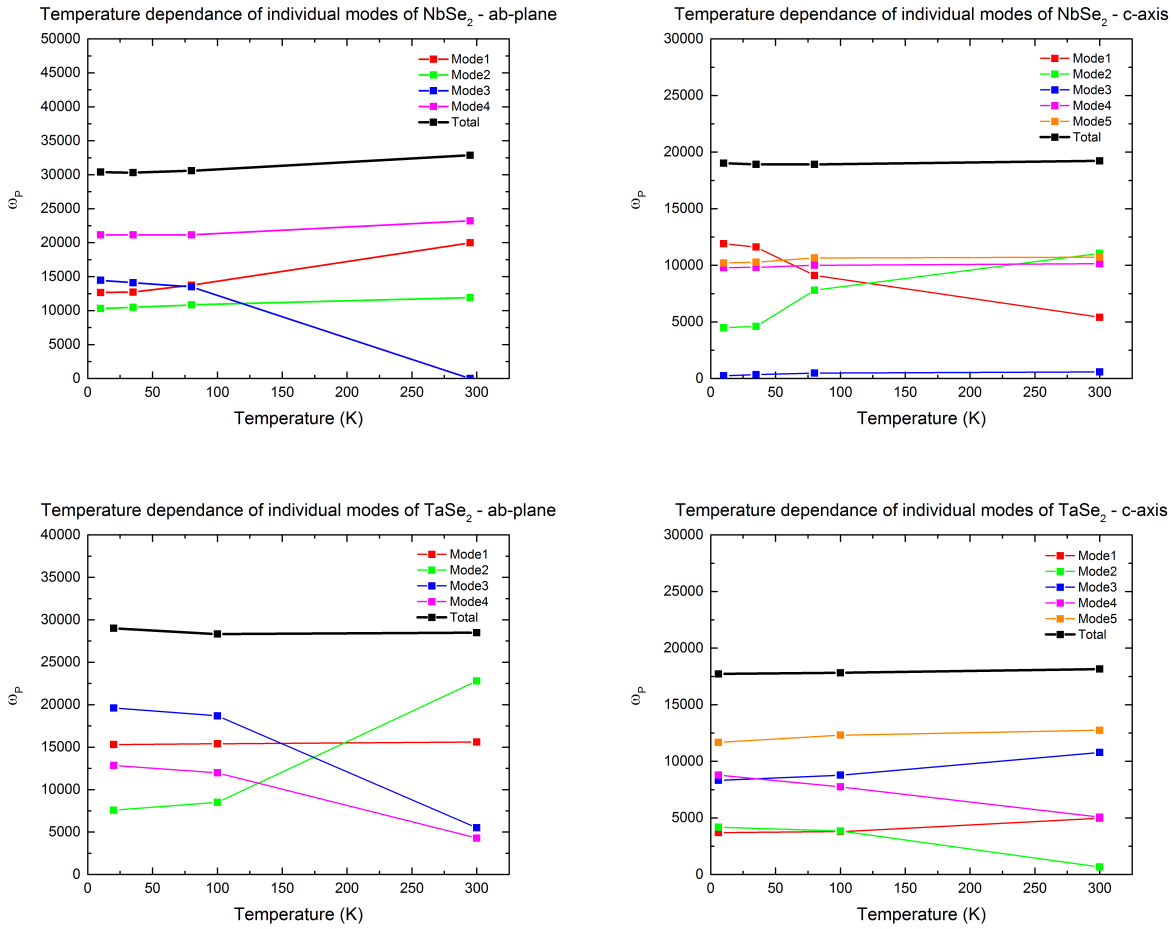

Figure 6.10: Plasma frequency (ω_P) of $NbSe_2$ and $TaSe_2$ as a function of temperature.

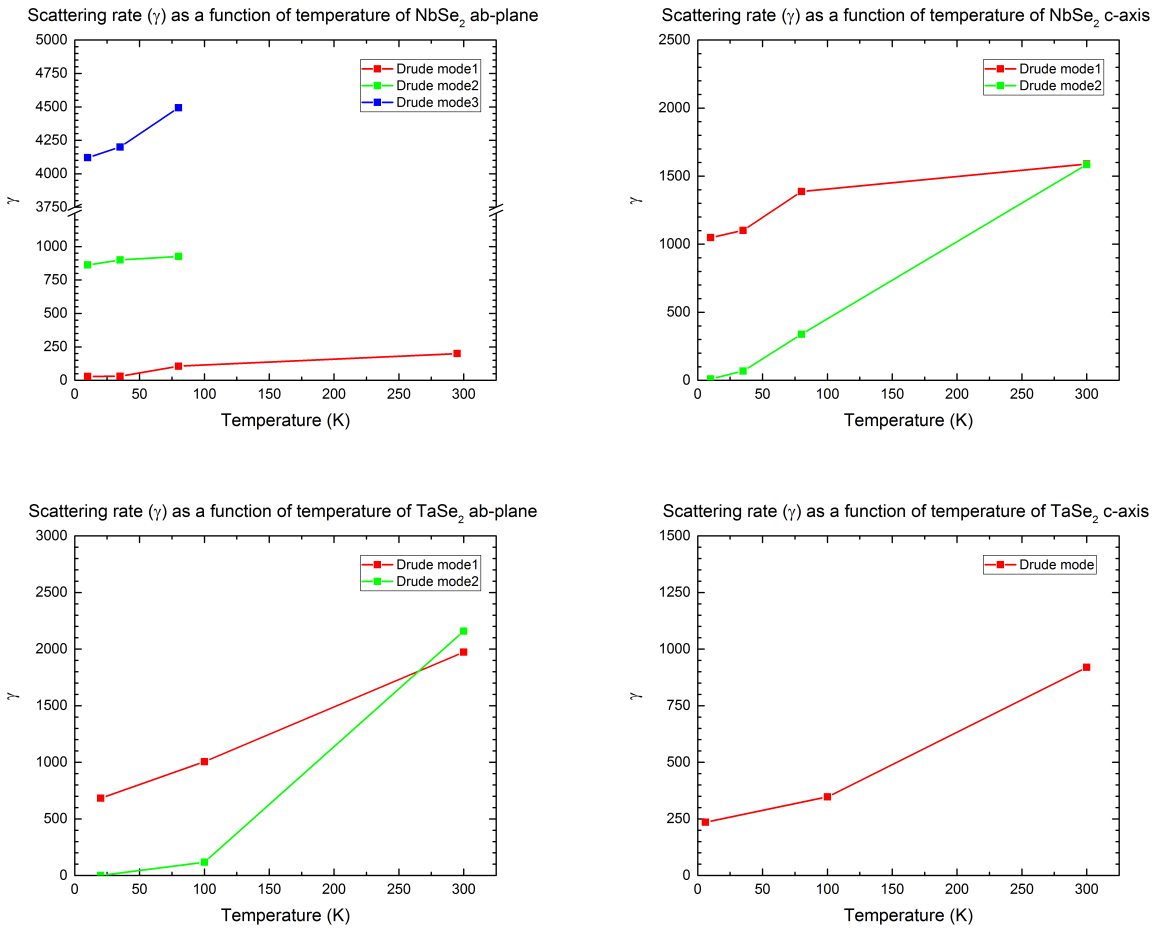

Figure 6.11: Scattering rate (γ) of $NbSe_2$ and $TaSe_2$ as a function of temperature.

When we consider plasma frequency as a function of temperature, the individual modes can be increased or decreased with temperature. Adding all the individual modes together gives the total plasma frequency. The total plasma frequency of the ab-plane or c-axis of the material remains constant. The graphs indicate that the total plasma frequency is nearly constant with the temperature; therefore the number of electrons remains constant since electrons cannot be created or destroyed.

$$\omega_p = \sqrt{\frac{Ne^2}{m^*\epsilon_0}} \tag{6.1}$$

Here N is the number density of electrons, e is the electric charge, m^* is the effective mass of the electron, and ϵ is the permittivity of free space.

The scattering rate (γ) is responsible for the linewidth of the reflectance graphs. In metals, the scattering rate decreases as temperature decreases. Only the Drude modes were used to fit the scattering rate graphs. The graphs of scattering rate as a function of temperature and the figures 2.2 and 2.3 are similar, and the resistivity of $NbSe_2$ and $TaSe_2$ decreses as temperature decreases. Drude mode 3 of $NbSe_2$ ab-plane, Drude mode 2 of $NbSe_2$ *c*-axis, Drude mode 1 of $TaSe_2$, and Drude mode of $TaSe_2$ *c*-axis are very similar to the resistivity graphs of $NbSe_2$ and $TaSe_2$. If we compare the scattering rate values, the scattering rate values of $NbSe_2$ for *ab*-plane are higher than the scattering rate values of $TaSe_2$ *ab*-plane. Scattering rate values of NbSe2 for *c*-axis are also higher than that of $TaSe_2$. Thus, the temperature dependence of resistivity is governed almost entirely on the scattering rate.

CHAPTER VII

CONCLUSION

In this work, we have analyzed mainly the reflectance data of anisotropic dichalcogenide systems 2H-$NbSe_2$ and 2H-$TaSe_2$ obtained using infrared spectroscopy and UV visible spectroscopy. We were able present a detailed study of their behavior across a large frequency range. The spectra of both materials show metallic behavior for both in-plane and intra-plane (within the ab-plane and along c-axis respectively).

The reflectivity of the ab-plane is greater than the reflectivity of the c-axis in both materials. If we compare the reflectivity of the ab-plane between both materials, 2H-$NbSe_2$ has the highest reflectivity for the ab-plane and the same is true for the c-axis. Also, the optical conductivity is higher in ab-plane than that of c-axis in both materials.

The reflectivity of a material depends on the collisions of the free electrons. According to the data analysis, the reflectivity decreases as the temperature increases because the collision of the free electrons increases with temperature. Once the incident frequency reaches the plasma edge the interband transition occurs and due to this process the conduction electrons increase. Thus, suddenly, the number of collisions in the conduction band increases, therefore decreasing the reflectivity decrease.

The anisotropy effects are more pronounced in 2H-$TaSe_2$ than 2H-$NbSe_2$.

The mean free path of an electron along the c-axis is shorter than the lattice spacing in the ab-plane. Hence the optical conductivity of these dichalcogenide materials is higher in ab-plane than the c-axis.

BIBLIOGRAPHY

[1] E.D. Palik. *Handbook of optical constants of solids.* El-sevier, Inc, academic press edition, 1985.

[2] E. Abrahams, S.V. Kravchenko, and M.P. Sarachik. Colloquium: Metallic behavior and related phenomena in two dimensions. *Reviews of modern physics*, 73:251, 2001.

[3] S.V. Dordevic, D.N. Basov, R.C. Dynes, B. Ruzicka, V. Vescoli, L. Degiorgi, H. Berger, R. Gaal, L. Forro, and E. Bucher. Optical properties of the quasi-two-dimensional dichalcogenides 2H-$TaSe_2$ and 2H-$NbSe_2$. *The European Physical Journal B*, 33:15–23, 2003.

[4] A. Zakery and S.R. Elliott. Optical properties and applications of chalcogenide glasses: a review. *Journal of Non-crystalline Solids*, 330:1–12, 2003.

[5] B Ruzicka, L. Degiorgi, H. Berger, R. Gaal, and L. Forro. Charge dynamics of 2H-$TaSe_2$ along the less-conducting c-axis. *Physical Review Letters*, 86, 2001.

[6] V. Vescoli, L. Degiorgi, H. Berger, and L. Forro. Dynamics of correlated two-dimensional materials: The 2H-$TaSe_2$ case. *Physical Review Letters*, 81, 1998.

[7] K. Yokota, G. Kurata, T. Matsui, and H. Fukuyama. Superconductivity in the quasi-two-dimensional conductor 2H-$TaSe_2$. *Elsevier*, 284-288:551–552, 2000.

[8] A. Soumyanarayanan, M.M. Yee, Y. He, J. Wezel, D.J. Rahn, K. Rossnagel, E.W. Hudson, M.R. Norman, and J.E. Hoffman. Quantum phase transition from triangular to stripe change order in $NbSe_2$. *PNAS*, 110:1623–1627, 2012.

[9] T. Yokoya, T. Kiss, A. Chainani, S. Shin, M. Nohara, and H. Takagi. Fermi surface sheet-dependent superconductivity in 2H-$NbSe_2$. *Science*, 294:2518–2520, 2001.

[10] S.V. Borisenko, A.A. Kordyuk, V.B. Zabolotnyy, D.S. Inosov, D. Evtushinsky, B. Buchner, A.N. Yaresko, A. Varykhalov, R. Follath, W. Eberhardt, and L. Patthey. Two energy gaps and fermi surface "arcs" in $NbSe_2$. *Physical Review Letters*, 102:166402–1 to 166402–4, 2009.

[11] A. LeBlanc and A. Nader. Resistivity anisotropy and charge density wave in 2H-$NbSe_2$ and 2H-$TaSe_2$. *ELSEVIER*, 150:1346–1349, 2010.

[12] C.C. Homes, M. Heker, Q. Li, Z.J. Xu, J.S. Wen, G.D. Gu, and J.M. Tranquanda. Determination of the optical properties of $La_{2x}Ba_xCuO_4$ for several dopings including anomolous x=1/8 phase. *physical Review B*, 13:85, 2012.

[13] A.P. Litvinchuk, C. Thomson, M. Cardona, and D.M. Ginsberg. Physical properties of high temperature superconductors iv. *World scientific*, singapore:375, 1994.

[14] W.Z.et al. Hu. Optical and raman spectroscopy studies of Fe-base superconductors. *Physica C*, 2009.

[15] S.V. Dordevic and D.N. Basov. Electrodynamics of correlated electron matter. *Ann. Phys.*, 15:545–570, 2006.

[16] N. Stojilovic, L. Konez, W. Kohlman, H. Rongwei, C. Petrovic, and S.V. Dordevic. Normal state charge dynamics of Fe 1.06 Te 0.88 S 0.14 super-conductor probed with infrared spectroscopy. *Physical review B-81*, 17, 2010.

[17] L. Nguyen, H.P. Komsa, E. Khestanova, R.J. Kashtiban, J.P.P. Peters, S. Lawlor, A. Sanchez, J. Sloan, R.V. Gorbachev, I.V. Grigorieva, A.V. Krasheninnikov, and S.J. Haigh. Atomic defects and doping of monolayer $NbSe_2$. *ACS Publications*, 11:2894–2904, 2017.

[18] K. Locharoenrat. *Optical Properties of Solids, An Introductory Textbook*. Pan Stanford Publishing Pvt.Ltd., Singapore, 2016.

[19] H. Gail and E. Sedlmayer. *Physics and Chemistry of Circumstellar Dust Shells*. Cambridge, Cambridge UP, 2014.

[20] F. Mark. *Optical Properties of Solids*. Oxford University Press, 2001.

[21] P. Griffiths and J. de Haseth. *Fourier Transform Infrared Spectrometry*. John Wiley and Sons, Hoboken, New Jersey, second edition, 2007.

[22] C. Kittel. *Introduction to Solid State Physics*. John Wiley and Sons, Inc, New York, 8th edition edition, 2005.

[23] M. Wolf. *Infrared and Optical Studies of Topological Insulators* Bi_2Te_3. MS thesis, The University of Akron, 2011.

[24] F. Salghetti-Drioli. *Magneto-Optical Kerr Effect in the Plasma-Edge Region: Evidence for Interplay between Drude Term and Interband Transitions*. Ph.D. thesis, Swiss Federal Institute of Technology Zurich, 1999.

[25] A. Kuzmenko. Guide to reffit software to fit optical spectra. Technical report, 2015.

[26] E. Abrahams, S.V. Kravchenko, and M.P. Sarachik. Metallic behavior and related phenomena in two dimensions. *Reviews of Modern Physics*, 73:251–265, 2001.